4 Three-dimensional density model of the Nazca plate and the Andean continental margin

Authors: Andrés Tassara, Hans-Jürgen Götze, Sabine Schmidt and Ron Hackney

Paper under review (September 27th, 2005) by the *Journal of Geophysical Research*

Abstract

We forward modelled the Bouguer anomaly in a region encompassing the Pacific ocean (east of 85°W) and the Andean margin (west of 60°W) between northern Peru (5°S) and Patagonia (45°S). The three-dimensional density structure used to accurately reproduce the gravity field is simple. The oceanic Nazca plate is formed by one crustal body and one mantle lithosphere body overlying a sub-lithospheric mantle, but fracture zones divide the plate into seven along-strike segments. The subducted slab was modelled to a depth of 410 km, has the same structure as the oceanic plate, but it is subdivided into four segments with depth. The continental margin consists of one upper-crustal and one lower-crustal body without lateral subdivision, whereas the mantle has two bodies for the lithosphere and two bodies for the asthenosphere that are separated across-strike by the downward prolongation of the eastern limit of active volcanism. We predefined the density for each body after studying its dependency on composition of crustal and mantle materials and pressure-temperature conditions appropriate for the Andean setting. A database containing independent geophysical information constrains the geometry of the subducted slab, locally the Moho of the oceanic and continental crusts, and indirectly the lithosphere-asthenosphere boundary (LAB) underneath the continental plate. Other geometries, especially that of the intracrustal density discontinuity (ICD) in the continental margin, were not constrained and are the result of fitting the observed and calculated Bouguer anomaly during the forward modelling. This contribution presents the model to the Andean geoscientific community and aims to serve as a tool for further interpretations. We discuss, within the restrictions imposed by a sensitivity analysis, some significant results in order to show the potential application of the model to the study of a wide range of Andean geodynamic processes. This includes: 1) Nature of the oceanic Nazca plate as constrained by its crustal thickness and mantle density structure; 2) Correlation between geometry of the slab and continental morphostructure, its relationship with subducted oceanic ridges and causes of flat subduction; 3) Depth to the continental LAB

as an indicator of the thermal regime and existence of lithospheric domains; 4) Moho depth, isostatic compensation of the orogen and continental-scale deformation mechanisms; 5) Geometry of the ICD mapping first-order variations in crustal structure, composition, temperature and partial melting degree along the margin.

4.1. Introduction

The Andean Cordillera is a continuous mountain chain along the western edge of South America that results from a uniform process of oceanic subduction underneath a continental margin. After 200 My of convergence this process has left a highly segmented margin, characterized by systematic along-strike variations in topography, morphology, tectonics, basin distribution, volcanism, subduction geometry, deep lithospheric structure and geologic history [e.g. Gansser, 1973; Jordan et al., 1983; Isacks, 1988; Mpodozis & Ramos, 1989; Cahill & Isacks, 1992; Dewey and Lamb, 1992; Kley et al., 1999; Gutscher, 2002; Jacques, 2003; Stern, 2004; Yáñez and Cembrano, 2004]. In order to define a primary framework and avoiding the differences between previous definitions, we propose the following boundaries and nomenclature for continental-scale segmentation (see inset of Fig. 4.1a): Northern (10°N-5°S), Central (5°S-33.5°S), Southern (33.5°-46.5°S) and Austral (46.5°-56°S) Andes.

The causes of this segmentation are not yet understood. Several authors argue that the correlation between features of the oceanic Nazca plate at the trench (age, subduction of ridges), along-strike changes in the shape of the subducted slab and boundaries of Andean segments (Fig. 4.1a) means that this segmentation is primarily controlled by the current configuration of the subducting plate [e.g. Jordan et al., 1983; Pilger, 1984; Pardo Casas y Molnar, 1987; Gutscher et al., 2000; Ramos et al., 2002; Yáñez et al., 2001, 2002; Lamb and Davies, 2003; Yáñez and Cembrano, 2004]. However, these segments and their boundaries are longstanding (10^8 yr) geological features of the Andean margin [e.g. Gansser, 1973; Mpodozis and Ramos, 1989; Mégard, 1984; Kley et al., 1999] that cannot by exclusively explained in terms of the current configuration of the oceanic plate. This is because such configuration changes during short-term (10^6-10^7 yr) plate reorganization processes, suggesting that the old structure of the continent should also play a role in controlling the fate of the Andean margin and the maintenance of its segmentation.

The evaluation of this hypothesis requires knowledge of the compositional structure of the convergence system at continental scales. We have tried to fulfil this requirement by

forward modelling the Bouguer anomaly for the Central and Southern Andes between 5° to 45°S and 60° to 85°W. The modelling area (Fig. 4.1a) encompasses parts of Peru, Brazil, Bolivia, Paraguay, Argentina, Chile and the Pacific Ocean. The main aim was to produce a model describing the three-dimensional (3D) density structure of the continental lithosphere, the Nazca plate and the subducted slab down to 410 km depth that can be used to analyse first-order structural and compositional variations along the continental margin. This goal was achieved without considering the details of regional and local structures but by producing a model that contain valuable information at the scale of the entire Andean margin.

After a brief revision of the Andean geotectonic framework, we describe the gravity database and methods used during this modelling. The latter includes a description of the rationale we followed to design the initial density structure, to allocate the density values for the bodies forming this structure and to define the reference density model used for the computation of the Bouguer anomaly generated by the model. We then present independent data (primarily a seismic database) that constrains the geometries of some density discontinuities contained in the 3D model. Considering the uncertainties and restrictions defined by a sensitivity analysis, we present and discuss the results of this modelling in terms of the main geometries of these discontinuities. In the final summary we suggest that this model will allow new insights into the structure of the western South American continental margin and the geodynamic processes acting along it.

4.2. Andean geotectonics

First-order geotectonic elements of the Nazca plate and the South American continent are shown in Fig. 4.1a. The age of the oceanic plate [Müller et al., 1997] along the Peru-Chile trench increases from 0 My at the triple junction with the Antarctic and South American plates (46.5°S, south of the area considered in this study) to a maximum of ~48 My around 20°S. North to this latitude the continental margin changes its orientation from NNE to NW, a feature known as the Arica Bend. The age of the oceanic lithosphere at the trench decreases to ~28 My at 5°S. Along-strike jumps in the age of the Nazca plate are associated with fracture zones recognisable as pronounced bathymetric lows with a general azimuth of ~70°. This is 10° lower than the average convergence direction defined by GPS measurements [e.g. Kendrick et al., 2003]. Bathymetric highs correspond to aseismic ridges (i.e. Nazca, Juan Fernández and Iquique) and to the active spreading center of the Chile Rise.

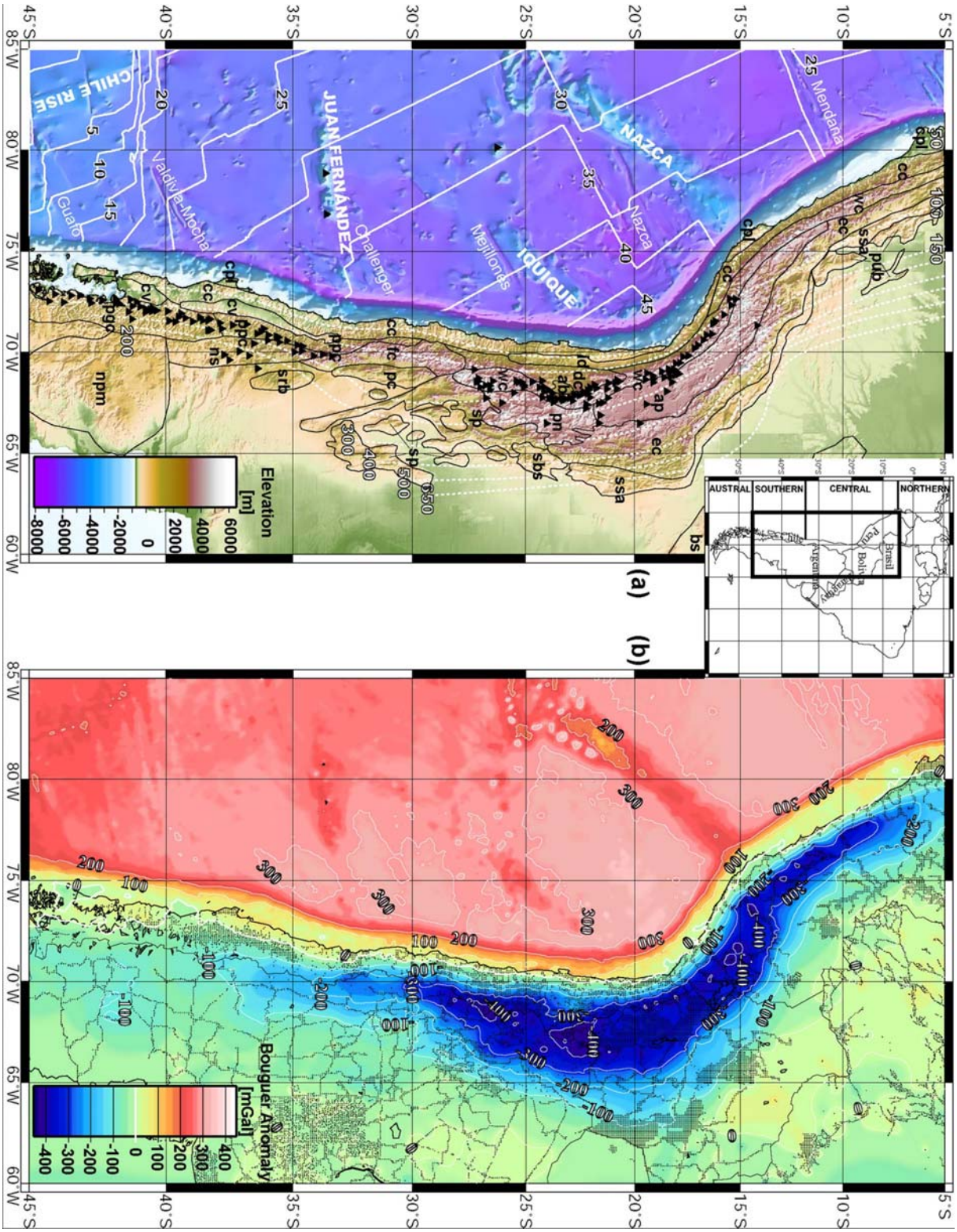

Fig. 4.1. Inset shows the study area (rectangle with bold lines) and continental-scale segmentation of the Andean continental margin. (a) Andean geotectonic setting on a digital elevation map. White lines in the offshore region, are isochrones of the Nazca plate [Müller et al., 1997] with ages in million of years, names in capitals denote aseismic ridges and the active spreading centre of the Chile Rise, names in minuscule denote fracture zones. In the onshore region, white dotted lines with numbers are isodepths [km] of the subducted slab from data available with GMT software package [Wessel and Smith, 1998], triangles are active volcanoes, black lines depict boundaries of morphotectonic units as modified after references cited in the text: cpl Coastal Plains, pub Peruvian Uplifted Blocks, cc Coastal Cordillera, id Intermediate Depression, cv Central Valley, dc Domeyko Cordillera, wc Western Cordillera, fc Frontal Cordillera, ppc Principal Cordillera, ab Atacama Basin, ap Altiplano, pn Puna, pc Precordillera, ec Eastern Cordillera, sp Sierras Pampeanas, ssa Sierras Subandinas, sbs Santa Barbara System, pgc Patagonian Cordillera, srb San Rafael Block, ns Neuquén System, npm North Patagonian Massif. (b) Bouguer anomaly map of the study region with contour lines every 100 mGal (1 mGal = 10^{-5} ms^{-2}). Dots in the onshore region depict the location of land gravity stations.

Contoured depth lines of the subducted slab [Cahill and Isacks, 1992; Creager et al., 1995; Gutscher, 2002], plotted in Fig. 4.1a for reference from data available with the Generic Mapping Tools [Wessel and Smith, 1998], show two segments of relatively flat subduction at intermediate depths (70-150 km) below Peru (5°-15°S) and Argentina (28°-33°S). The spatial correlation with the subduction of the Nazca ridge at 15°S and the Juan Fernández ridge at 33°S suggests a causative relationship with the development of these flat-slab segments [e.g. Gutscher et al, 2000; Yáñez et al., 2002]. For the rest of the region, the slab subducts with a dip angle of 25-35° until ~200 km, increasing at greater depths.

Fig. 4.1a also shows the position of modern volcanoes and morphotectonic units forming the continental margin. Based on the propositions of Jordan et al. [1983], Mégard [1984], Mpodozis and Ramos [1989], Allmendinger et al. [1997] and Kley et al. [1999], these morphotectonic units have been redrawn using a GIS-based analysis of digital topography and digital geological databases of South America [Schobbenhaus and Bellizzia, 2001], Argentina [SEGEMAR, 1998] and Chile [SERNAGEOMIN, 2003]. The Andean forearc is dominated by the Coastal Cordillera. Along segments with steep subduction, this unit is separated from the high internal cordilleras by forearc basins (Intermediate Depression and Central Valley). Some uplifted Coastal Plains form notables peninsulas disturbing the otherwise smooth coastline (e.g Mejillones and Arauco peninsulas). The offshore forearc is very steep in between the subduction points of the Nazca and Juan Fernández ridges, but has a more subtle bathymetry and contains submarine basins to the north [e.g. Clift et al., 2003; Krabbenhöft et al., 2004] and south [e.g. Bangs and Cande, 1997] of this area.

The Central Andes are a huge mountain range, covering an area of ~800,000 km^2 above an elevation of 3500 m. The morphology is dominated by the Altiplano-Puna plateau with a maximum width of ~400 km at 18.5°S. North and south of the plateau, the high cordilleras narrow to less than 200 km width. This narrowing correlates with a decrease in Neogene crustal shortening [e.g. Isacks, 1988; Kley et al., 1999; Hindle et al., 2005], which itself is related to systematic changes in the deformation style of the foreland: Thin skinned along the Sierras Subandinas, thick skinned along the Santa Barbara System and the northern Eastern Cordillera, and basement uplift along the Sierras Pampeanas and Peruvian Uplifted Blocks [e.g. Kley et al., 1999]. The absence of asthenospheric mantle above flat-slab segments precludes the occurrence of arc magmatism and hence the Central Volcanic Zone (CVZ) of the Andes is restricted to the Western Cordillera between 15° and 28°S. The CVZ is composed of andesitic-dacitic calc-alkaline stratovolcanoes and bi-modal volcanic products deposited on the Altiplano and Puna [e.g. Allmendinger et al., 1997].

The borderline between the Central and Southern Andes at 33.5°S is a major tectonic transition [e.g. Yáñez et al., 2002] bounding almost all the morphotectonic units exposed in this region (Fig. 4.1a). South of this latitude, elevations higher than ~4000 m decrease gradually along the Principal Cordillera to less than 2000 m at the Patagonian Cordillera. This decrease also correlates with north-south variations in the Neogene tectonic style. Basin inversion along the Principal Cordillera and thick-skinned foreland tectonics along the Neuquén System are linked with trench-oblique structures [Godoy et al., 1999; Charrier et al., 2002; Cobbold and Rossello, 2003]. These styles change south of 38°S to trench-parallel, dextral strike-slip along the Liquiñe-Ofqui Fault Zone (LOFZ) with dominant forearc extension and little shortening recorded along the Patagonian Cordillera and the North Patagonian Massif [e.g. Lavenu & Cembrano, 1999; Folguera et al., 2004; Diraison et al., 1998]. The steep subduction of the oceanic slab drives the mantle magmagenesis feeding the Southern Volcanic Zone (SVZ). The northern part of the SVZ, atop the Principal Cordillera, is composed of andesitic calc-alkaline stratovolcanoes with a crustal magmatic component decreasing southward [e.g. Hildreth and Moorbarth, 1988]. The southern SVZ (south of 39°S) builds the western-central part of the Patagonian Cordillera and is genetically related to the LOFZ [Hervé, 1994; Lopez-Escobar et al., 1995; Cembrano et al., 1996]. This volcanic chain is composed of andesitic and basaltic stratovolcanoes of calc-alkaline to tholeitic affinities and several minor eruptive centres [e.g. Lopez-Escobar et al., 1995].

4.3. Bouguer anomaly database

The Bouguer anomaly for a point on the Earth's surface is the difference between the observed value of gravity acceleration and a theoretical value at that point. This theoretical value is derived from gravity on the ellipsoid corrected to the elevation of the point and by accounting for the rock masses between the ellipsoid and the measurement point. The Bouguer anomaly reflects mass deficits (negative values) and surpluses (positive values) with respect to a normal Earth density structure.

Offshore Bouguer anomalies have been computed from the KMS01 satellite-derived free-air anomaly database (Andersen et al. [2001]; ftp://ftp.kms.dk/GRAVITY) by applying a correction using digital bathymetric data (http://www.ngdc.noaa.gov/mgg/gebco) on a 2´ grid and replacing the water layer with material of density 2.67 Mg/m^3. Onshore gravity data for the South American continent have been recently compiled, homogenized and processed by the Escola Politecnica Universidade de São Paulo (Brazil). The database was provided to us by Dr. Denizar Blizkow (pers. comm.) in the framework of a cooperation agreement with the

German Collaborative Research Centre SFB267 “Deformation Processes in the Andes” (hereafter SFB267). We use the Bouguer anomaly of circa 20,000 stations covering the study area (dots in Fig. 4.1b), as originally reported in this database. Marchenko [in prep.], who exploited these data to compute a geoid model for the continent and surrounding oceans, estimate an average error in the onshore free-air anomaly to be ca. 10 mGal (1 mGal = 10^{-5} m/s^2). We assume that the further reduction to the Bouguer anomaly has expanded this error to an average uncertainty of ±20 mGal.

Combining both databases, we generated the Bouguer anomaly map of Fig. 4.1b. It shows a pronounced negative anomaly less than –200 mGal associated with the high cordilleras of the Central Andes. This anomaly decreases locally to less than –400 mGal along portions of the Western Cordillera. A minimum of ca. –450 mGal is located around the boundary between the Altiplano and Puna. Along the Southern Andes the Bouguer anomaly is greater than –200 mGal and increases to the south. South of 38°S the anomaly is no longer correlated with the cordilleras and its minimum (ca. –120 mGal) is located on the North Patagonian Massif.

The 0 mGal contour coincides with the coastline along the Peruvian forearc, whereas in Chile it is shifted landward. This is more obvious south of 25°S and particularly along the Southern Andes where this contour follows the limit between the Coastal Cordillera and the Central Valley (exceptions occur around 39°S and 43°S). Positive Bouguer anomalies are observed along the Andean foreland between 38° to 25°S and north of 15°S. They also dominate the offshore gravity field. The trench axis correlates with the 200 mGal contour line and a strong positive gradient to the west. (Hereafter the terms very short, short, intermediate and long wavelengths are used respectively for wavelengths <100 km, 100-300 km, 300-1000 km and >1000 km.) Maximum Bouguer anomalies of circa 350 mGal are observed together with less positive anomalies as spots of very short wavelength along the south-western limit of the Nazca ridge. In general, oceanic ridges and fracture zones are characterized by regions of less pronounced positive anomalies than their surroundings. Segments of oceanic lithosphere separated by fracture zones show maximum Bouguer anomalies along an outer rise west of the trench and a general increase in the magnitude of the anomaly from north and south toward a region between the Nazca and Iquique ridges. This spatial variation is positively correlated with the age of the Nazca plate.

4.4. 3D density model

Forward modelling of the Bouguer anomaly was performed using the in-house software IGMAS, which stands for “Interactive Gravity and Magnetic Application System” (http://www.gravity.uni-kiel.de/igmas). The modelling software [Götze, 1984; Götze and Lahmeyer, 1988; Götze and Schmidt, 1997; Schmidt and Götze, 1998; Breunig et al., 2000] makes use of an interoperable 3D Geoinformation System (IOGIS) and its functionality [Breunig et al., 2000]. The model is formed by three-dimensional bodies that are constructed using polyhedra whose geometry is predefined by the user on a series of parallel vertical cross-sections. Density values for the modelled bodies are also defined prior to the gravity modelling. IGMAS enables the user to consider all available digital constraining data in the 3D space. By iteratively changing the geometry of the initial structure along each cross-section in accordance with the existing constraining information, the user eventually converges to the optimal fit between the observed Bouguer anomaly and that produced by the modelled 3D density structure. This modelled anomaly is calculated considering the density contrast between values given to the modelled bodies and those of a reference model. Thus, the design of a 3D density model in IGMAS incorporates three important decisions: the definition of the initial structure, the selection of density values for the bodies forming the model and the choice of a reference model. The rationale, data and procedures allowing these decisions to be made are described below.

4.4.1. Initial model structure

The observed correlation between the Bouguer anomaly and the age of the Nazca plate suggests that the density structure of the oceanic lithosphere is dominated by the age discontinuities associated with fracture zones. Because of this we defined the vertical cross-sections of the model in a direction parallel to these fracture zones. Fig. 4.2a shows the 43 sections that comprise the model. They are separated by 1° in latitude, have a length of ca. 3000 km in the central part of the model and a depth of 410 km (upper mantle discontinuity). Bold lines in Fig. 4.2a are profiles roughly coinciding with the six first-order fracture zones labelled in Fig. 4.1a. In the model, segments of the oceanic lithosphere and the slab with a distinctive density structure are in contact across these fracture zones. The resulting seven segments are labelled with roman numbers in Fig. 4.2a.

Fig. 4.2b shows one of the 43 modelled cross-sections as an example of the initial structure used to construct this model. This structure is simplified with respect to the complexity expected for subduction zones, but it is sufficient to fill the main aim of this

modelling effort, i.e. the description of the density structure of the convergence system at continental scales.

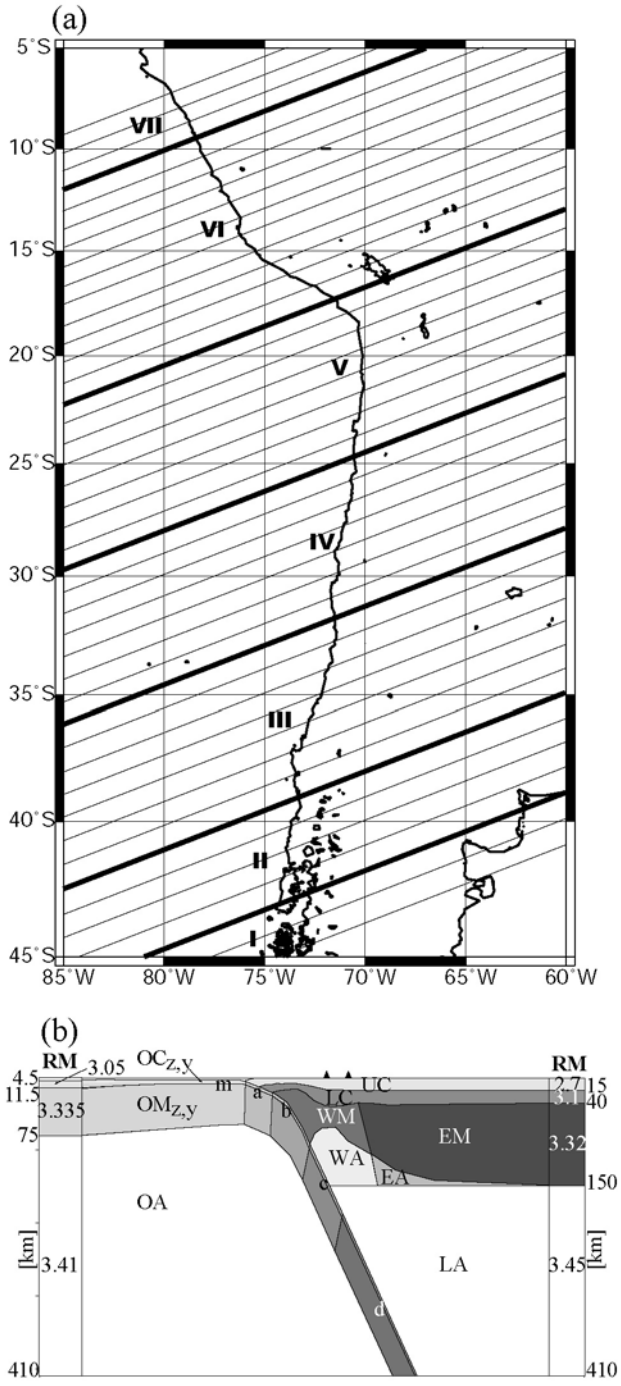

Fig. 4.2. (a) Distribution of the 43 vertical cross-section from which the three-dimensional density structure of the model is triangulated. Thick lines coincide with fracture zones from Plate 1a and correspond to cross-sections dividing the density structure of the oceanic plate and subducted slab in seven segments that are labelled with roman numbers I to VII. (b) One of the vertical cross-sections showing the downward extension of the model till 410 km and its general density structure. 4-times vertical exaggeration. Triangles represent volcanoes. Columns along figure's extreme labelled RM represent the reference density model with values in Mg/m^3. Abbreviations of bodies and their densities are defined in Table 1. See text for description.

The oceanic plate and slab are formed by a one-layer crust ($OC_{z,y}$) overlaying a mantle lithosphere body ($OM_{z,y}$). In Fig. 4.2b, the suffix *z* is equal to *m* for the marine part of the oceanic plate and *a* to *d* for the subducted parts of the slab. This division allows for downward densification of the slab. The suffix *y* takes values between I and VII along the strike of the

study area (Fig. 4.2a). The oceanic plate and slab are underlain by one body representing the asthenospheric mantle (OA in Fig. 4.2b).

The continental plate is formed by a two-layer crust (UC and LC in Fig. 4.2b) overlying a mantle lithosphere. The crustal structure is unrealistic because it doesn't account for the complex vertical stratification of the crust observed worldwide [e.g. Christensen and Mooney, 1995], nor for the lateral variation of upper and lower crustal density that is very likely in a region extending more than 4000 km that is characterized by a complex surface geology. Note, however, that our intention is to use the depth to the intracrustal density discontinuity (ICD) separating light upper crustal material to dense lower crust as a proxy for this complex density structure.

The continental mantle lithosphere is formed by two bodies whose boundary is located underneath the easternmost active volcano observed within 50 km of each modelled section (the position of active volcanoes is taken from the database of the Smithsonian Institute; http://www.volcano.si.edu/gvp/world). The eastern lithospheric body (EM in Fig. 4.2b) represents the relatively cold and dense mantle below the Andean foreland and shield regions. The western lithosphere (WM in Fig. 4.2b) should be less dense because it underlies the hot volcanic arc and is presumably hydrated underneath the forearc region. Below the lithosphere-asthenosphere boundary (LAB), asthenosphere shallower than 150 km is also formed by two bodies (WA and EA in Fig. 4.2b) separated by the downward projection of the easternmost volcano on each section. These bodies attempt to represent the expected gradual decrease in asthenospheric density toward the volcanic arc produced by high temperatures and hydration of the wedge. The subcontinental mantle below 150 km depth is represented by one body of constant density (LA in Fig. 4.2b). The depth of 150 km was selected based on the results described in appendix A and discussed below.

4.4.2. Reference density model

The main objective of this modelling is to study the density structure underneath the continental margin. Therefore, we choose a reference model typifying the density variations with depth in a column of average continental lithosphere. This is represented by the right column in Fig. 4.2b, which is identical to the initial structure along the eastern side of each cross-section of the 3D model. The reference model as an intracrustal density discontinuity (ICD) at 15 km, Moho at 40 km and lithosphere-asthenosphere boundary (LAB) at 150 km. The crustal structure is consistent with the global compilation of refraction seismic profiles of Christensen and Mooney [1995] that characterize the structure of the continental crust

worldwide. In appendix A, we briefly analyse the thermal and density structure of the mantle. We found that for an average surface heat flow of 50 mW/m^2 along the Andean distal foreland-shield region [Hamza and Muñoz, 1996; Springer and Föster, 1998], the LAB depth should be 150 km (Fig. 4A.2b of appendix A). Following the results discussed by Tassara [submitted paper], a density of 2.7 Mg/m^3 characterizes an upper crust formed by granites with 73 wt% SiO_2, whereas a lower crustal density of 3.1 Mg/m^3 has diverse interpretations. For normal crustal thickness (~35-40 km), this value represents the average density of an anhydrous gabbro or a more basic, but hydrated, mafic amphibolite; if the lower crust were buried to greater depths (like in the Andean crustal roots) this value is representative of meta-igneous rocks with an andesite to basaltic-andesite composition, independently of their hydration degree (see Tassara [submitted paper] for a complete discussion of these issues). The density selected for the reference mantle lithosphere is 3.32 Mg/m^3. As shown in Fig. 4A.2b of appendix A, this value is an average of those expected for a common continental harzburgite for surface heat fluxes normal of foreland-shield regions (45-55 mW/m^2; e.g. Hamza and Muñoz, 1996). A density of 3.45 Mg/m^3 for the sublithospheric mantle in the reference model is an average of values computed in appendix A (Fig. 4A.1) for a pyrolite mantle along an adiabatic thermal gradient between the LAB depth of the reference model (150 km) and the bottom of the model at 410 km depth.

The reference model, resembling the density structure of continental regions with a surface heat flow of ~50 mW/m^2, defines a total mass of 1.38x10^9 kg along a vertical column with a volume equal to 1 m^2 x 410 km. This is the same mass that would be contained in a similar column below an ocean whose lithosphere formed at 30 Ma (left column in Fig. 4.2b) if the following conditions are met: 1) the thermal structure of the oceanic plate is described by a plate-cooling model [Turcotte and Schubert, 2002, p. 176] leading to a water depth of 4.5 km and a LAB depth of 75 km (Fig. 4A.2a), 2) the oceanic crust has a normal thickness of 7 km [e.g. Bown and White, 1994] and a density of 3.05 Mg/m^3, 3) both the mantle lithosphere and asthenosphere are formed by a fertile lherzolite, in which case the average densities for this plate age are 3.335 Mg/m^3 and 3.41 Mg/m^3, respectively (Fig. 4.2b, Fig. 4A.2a). In this scenario, the selected reference model also represents the density structure of an oceanic plate whose age is the average of the Nazca plate age along the model region (Fig. 4.1a). Note that continental regions that are nominally similar to the reference model in that the measured heat flow is ~50 mW/m^2, like in the northeast corner of the model region [Hamza and Muñoz, 1996], are effectively characterized by an observed Bouguer anomaly near 0 mGal (see Fig. 4.1b). This indicates that the reference model is a good representation of stable, “non-

anomalous" continental areas. However, zones of the oceanic plate with an age of 30 Myr show Bouguer anomalies between 250 and 300 mGal (Fig. 4.1) because the computation of these anomalies offshore has replaced ocean water by material with density 2.67 Mg/m^3. Using the same density for the water layer in the 3D model we are confident that the Nazca plate density structure resulting from the modelling is consistent with the expectations of an age-dependent plate-cooling model.

4.4.3. Selection of density values for modelled bodies

We predefined the density for each of the bodies forming the 3D model after studying the dependency of this physical parameter on composition, water content and pressure-temperature conditions of crustal and mantle materials that are appropriate for the Andean geodynamic setting. We make use of some analytical tools, including those presented by Tassara [submitted paper] for the continental crust and in appendix A for the mantle, which support the choice of the density values summarized in Table 1, as discussed next.

Table 1: Densities [Mg/m^3] selected for the bodies forming the 3D model

Segment	Oceanic Plate and Subducted Slab										Continental Plate				Asthenosphere			
	m		a		b		c		d									
	OC	OM	OC	OM	OC	OM	OC	OM	OC	OM	UC	LC	WM	EM	OA	LA	WA	EA
I	2.98	3.26	2.98	3.26	3.25	3.30	3.35	3.38	3.55	3.5	2.7	3.1	3.24	3.32	3.41	3.45	3.31	3.35
II	3.00	3.30	3.00	3.30	3.2	3.33	3.3	3.4	3.55	3.5								
III	3.05	3.33	3.05	3.33	3.2	3.36	3.3	3.4	3.55	3.5								
IV	3.05	3.34	3.05	3.34	3.2	3.36	3.3	3.4	3.55	3.5								
V	3.05	3.355	3.05	3.355	3.2	3.37	3.3	3.4	3.55	3.5								
VI	3.05	3.35	3.05	3.35	3.2	3.36	3.3	3.4	3.55	3.5								
VII	3.05	3.34	3.05	3.34	3.2	3.36	3.3	3.4	3.55	3.5								

Abbreviations: I-VII; along-strike segments of the oceanic plate and subducted slab; m = marine part of the oceanic lithosphere; a-d = downward parts of the slab; OC = oceanic crust; OM = oceanic mantle lithosphere; UC = upper continental crust; LC = lower continental crust; WM = western continental mantle lithosphere; EM = eastern continental mantle lithosphere; OA = oceanic asthenosphere; LA = lower continental asthenosphere; WA = western continental asthenosphere; EA = eastern continental asthenosphere.

4.4.3.1.Nazca plate

Hacker et al. [2003a] estimated values of physical parameters (including density) of subduction zone rocks based on a compilation of physical properties for minerals composing these rocks and the construction of phase diagrams representative of their metamorphic PT conditions. Fig. 4.3 summarizes the density values calculated by these authors for metamorphosed and fresh MOR-basalts (Fig. 4.3a) and harzburgite mantle (Fig. 4.3b) for temperatures between 100° and 1000°C and pressures up to 8 GPa (~270 km depth). At near-seafloor conditions (bottom-left corner of Fig. 4.3a) a fresh oceanic crust would have a density of 3.1 Mg/m^3, whereas its fully hydrated counterpart shows a reduced density of 2.7

Mg/m^3. The density of 3.05 Mg/m^3 we have selected for the oceanic crust of the reference model and segments IV to VII of the Nazca plate implies a mixture of 85% fresh basalts and gabbros and 15% fully metamorphosed basalts that is consistent with seismic findings worldwide [e.g. Carlson and Miller, 2004]. The reduction of the crustal density for the three southernmost segments (I to III, Table 1) is necessary for achieving a fit with the observed Bouguer anomaly near the trench axis. This reduction suggests either an intrinsically low crustal density, consistent with these segments being created at the slow-spreading Chile Rise [Henstock and Thompson, 2004], or the existence of cracks that are still open and filled with seawater because the relative young age of these segments precludes their closure [e.g. Carlson, 2004].

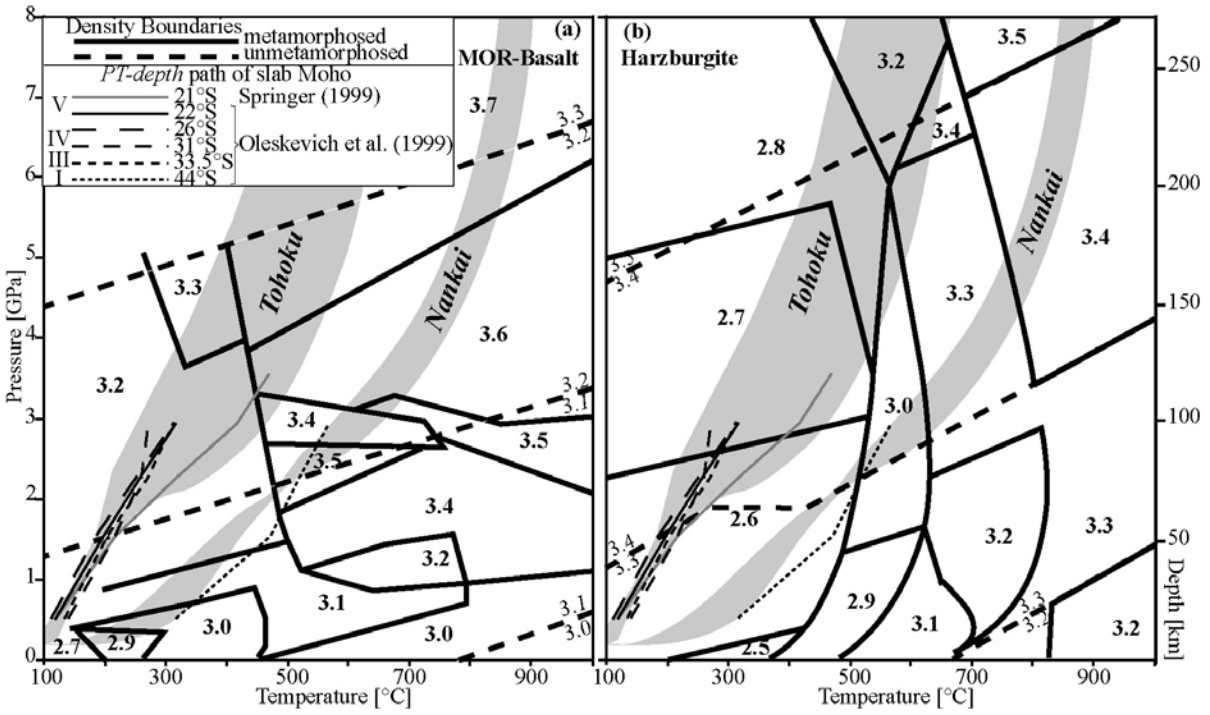

Fig. 4.3. Pressure-Temperature-Depth diagrams and boundaries of density fields associated with metamorphic facies for (a) MOR-basalt and (b) Harzburgite, after Hacker et al. [2003a]. Density boundaries are shown by thick lines; bold for metamorphosed rocks and segmented for un-metamorphosed rocks, with density values in Mg/m^3. Thin lines are PT-depth paths of oceanic Moho for some Andean profiles proposed by Springer [1999] and Oleskevich et al. [1999]. Grey regions labelled Tohoku and Nankai after Hacker et al. [2003a].

Information summarized in Fig. 4A.2a of appendix A, together with the age distribution of the Nazca plate [Müller et al., 1997], was used to initially fix the thickness and density of the oceanic mantle lithosphere at the trench for each of the seven segments forming the Nazca plate in the model. However, the final density values selected for each body were fine tuned during the modelling in order to fit the observed long-wavelength Bouguer anomaly near the trench axis. The final density values for each segment are shown in Table 1.

4.4.3.2.Subducted slab

The densification of the slab with depth that drives plate tectonics is the result of metamorphic reactions occurring in the oceanic crust and mantle lithosphere as they are exposed to high temperatures and pressures during passage toward the deep mantle [e.g. Kirby et al., 1996; Peacock and Wang, 1999; Hacker et al., 2003a]. Understanding these reactions and their effect on the density structure of the subducted Nazca slab is restricted by the incomplete knowledge of the thermal structure of the Andean subduction zone. Springer [1999] and Oleskevich et al. [1999] proposed two-dimensional temperature profiles along some specific regions of the Central and Southern Andean forearc. From these profiles we have extracted the (P)T-depth path of the slab Moho and plotted them in the diagrams of Fig. 4.3. This information was used to gain insights into the probable changes in slab density with depth and to select the density values for crustal and mantle bodies of the slab segments *a* to *d* (Fig. 4.2b, Table 1). In particular, it can be observed (Fig. 4.3) that for relatively old segments of the Nazca slab (III to V; 33.5°S to 21°S) the PT-depth paths down to 100 km depth are very similar to each other and also to that of the old Pacific slab subducting along the Tohoku trench (NE Japan; Peacock and Wang [1999] and Hacker et al. [2003a]). For these slabs, a relatively smooth increase in density is expected with depth, in contrast to the situation of the young and warm slab subducting at 44°S (segment I) which is comparable to the Philippine slab below Nankai (SW Japan; Peacock and Wang [1999] and Hacker et al. [2003a]). The high temperatures reached at shallow depths in these subduction zones imply an important increase in density at depths less than 100 km due to the enhanced dehydration of mostly the oceanic crust. Without a better understanding of the thermal structure along the Andean subduction zone, we consider the proposed density structure of the slab (Table 1) as a roughly but acceptable first approximation.

4.4.3.3.Continental margin

Along the entire study region the crust is formed by two layers whose densities remain unchanged with respect to the values selected for the reference model (i.e. 2.7 Mg/m^3 for the upper crust and 3.1 Mg/m^3 for the lower crust). The expected spatial variation of the crustal density structure with respect to the reference model, mostly caused by lateral changes in crustal composition and thermal conditions [Tassara, submitted paper], is represented in this modelling by variations in the depth of the Intracrustal Density Discontinuity (ICD).

The eastern mantle lithosphere (EM in Fig. 4.2b and Table 1) maintains a density of 3.32 Mg/m^3, as in the reference model. However, toward the active volcanic arcs the heat flow increases and this latter value is not realistic. Considering the information summarized in appendix A, the selected density for the western mantle lithosphere body (WM in Fig. 4.2b and Table1) is 3.24 Mg/m^3. This value accounts for the very high heat flow observed along Andean volcanic arcs [Henry and Pollack, 1988; Hamza and Muñoz, 1996; Springer and Förster, 1998]. Note also that this body underlies the forearc region and hence it should include the effect of the extensive hydration likely produced by water liberated from the subducting slab. For the range of depths (30 to 100 km) and temperatures (150° to 600°C) expected for the Andean mantle forearc [e.g. Oleskevich et al., 1999], Fig. 4.3b predicts that a fully hydrated, serpentinized harzburgite should have an average density near 2.7 Mg/m^3, whereas a fresh harzburgite would show an average density of 3.35 Mg/m^3. The selected value of 3.24 Mg/m^3 implies a mixture of 20% of the former with 80% of the latter. These relative proportions are consistent with the percentage of serpentinization of the mantle forearc deduced from seismic studies worldwide [Carlson and Miller, 2003].

In order to include the likely reduction of mantle density toward the asthenospheric wedge, the 3D model considers two bodies (WA and EA in Fig. 4.2b and Table 1) between the LAB depth of the reference model (150 km) and the modelled continental LAB. As shown in Fig. 4A.2b of appendix A, the density of 3.35 Mg/m^3 selected for the eastern asthenosphere body is an average of the values expected for a mantle lithology characterized as a fertile and hence dense lherzolite and for heat fluxes lower than 70 mW/m^2. The western asthenosphere below active volcanic zones, where the heat flow is higher than 75 mW/m^2 [Hamza and Muñoz, 1996; Springer and Förster, 1998], can be represented by a density of 3.31 Mg/m^3 that is slightly lower than the reference lithospheric mantle.

4.5. Geometry of density discontinuities and their constraints

Once the initial model structure was defined, the reference model chosen and the density values for the modelled bodies selected, ~250 hours were used to locate the density discontinuities in accordance with all available constraining information and to iteratively modify the geometries of unconstrained discontinuities in order to fit the observed and modelled Bouguer anomaly. In order to minimize the intrinsic non-uniqueness associated with potential field forward modelling, we compiled an updated database containing seismic information mostly produced during experiments carried out by the SFB267, but also including results published by other authors for regions outside the working areas of this

project. These data were loaded into the model to constrain the geometry of the subducted slab along the entire study region and the oceanic and continental Moho at some specific locations. Other published information was used to indirectly constrain the geometry of the continental LAB.

4.5.1. Oceanic plate

The oceanic crustal thickness was initially fixed to 7 km, the average global value [White et al., 1992; Bown and White, 1994], but during modelling the oceanic Moho was adjusted to match the local constraints given by refraction seismic profiles for some regions near the trench axis (Fig. 4.4) and mostly by fitting the short to intermediate wavelength Bouguer anomaly along the modelled cross-sections.

For each segment forming the Nazca plate, our model represents the oceanic mantle lithosphere with one body whose thickness and density were initially forced to correspond with the age-predicted values at the trench axis. These predicted values were computed as described in appendix A using the Nazca age grid of Müller et al. [1997]. These initial values were then optimised for an area near the trench axis in order to fit the intermediate to long wavelength Bouguer anomaly there. Fig. 4A.2a (appendix A) shows that a decrease in Nazca ages west of the trench implies not only a reduction in the age-predicted LAB depth in that direction but also a subsequent decrease of the average lithospheric density with respect to the value at the trench. This density decrease is the result of hotter thermal conditions for younger plate ages. Therefore, a westward-increasing lithospheric mass deficit with respect to the density structure at the trench can be predicted by the plate-cooling model, something that is consistent with an offshore Bouguer anomaly decreasing toward the west (Fig. 4.1b). With only one body of constant density representing the oceanic lithosphere in the model, we reproduce this pattern by replacing westward-increasing amounts of dense sub-lithospheric mantle by lighter lithospheric material to fit the long wavelength Bouguer anomaly.

4.5.2. Subducted Nazca slab

The Moho and upper surface of the slab have been imaged by reflection and refraction seismic profiles along some regions of the forearc. Receiver function studies also locally image the slab Moho. From the references listed in Fig. 4.4, we digitized the depth to these discontinuities and included them into the model. This information was combined with hypocenters recorded by local seismic networks (as referenced in Fig. 4.4) and complemented with seismicity registered at teleseismic distances. This latter information has been obtained

from three different sources: The USGS NEIC catalogue (http://neic.usgs.gov/neis/epic/), the "Centennial Global Earthquake Database" (http://www.geonavi.com/eric/HotNews/eqDB.html) and data described by Engdahl et al. [1998]. The digitized seismic images and the seismicity associated with the Wadati-Benioff zone were used to locate the upper surface of the slab. To do that, data within 50 km of each modelled cross-section were considered. Selected profiles of the global tomography model of Villaseñor et al. [2003] were used to constrain the main geometry of the slab at depths greater than 200 km, where seismicity is generally scarce.

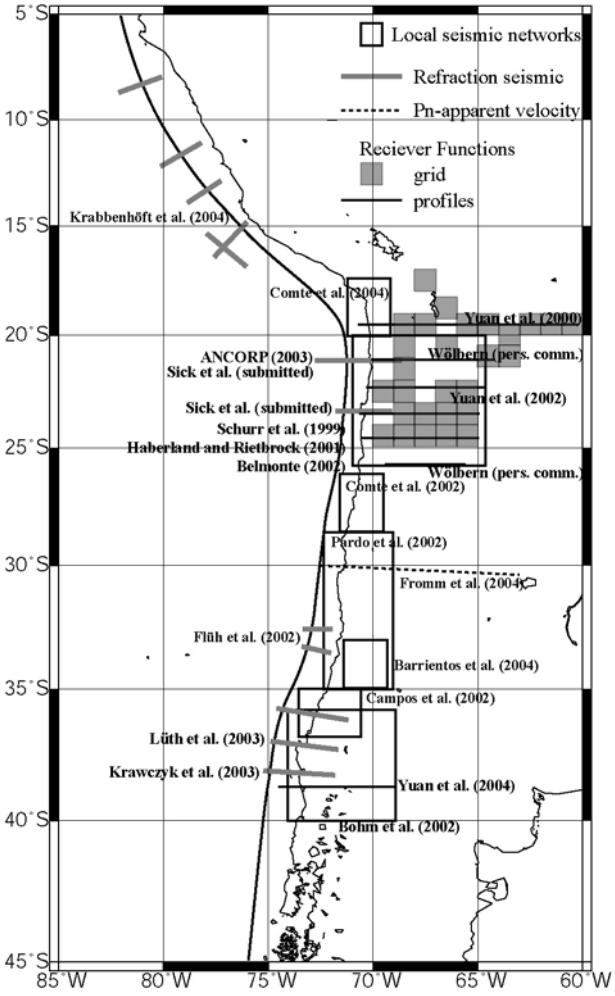

Fig. 4.4. Distribution and references of locally-generated seismic information incorporated into the 3D density model to constraint the geometry of the subducted slab (local seismic networks and refraction seismic profiles) and the continental Moho (Pn-apparent velocity and Receiver Functions results).

The resulting slab geometry is best constrained along regions like the Central Andes between 20° and 25°S where seismic profiles, receiver functions observations and local seismic networks are available and the global tomography model is well constrained. For these regions we estimate an uncertainty of ±5 km at 150 km depth based on the standard average error for hypocenter locations [e.g. Hacker et al., 2003b]. However, the slab geometry

is poorly defined in other regions, like the Southern Andes south of 40°S, where no local data are available, teleseismic information is intrinsically scarce at all depths, and the global tomography model is poorly resolved. Along this latter region uncertainties, can be as high as ±25 km at 150 km depth.

4.5.3. Continental lithosphere-asthenosphere boundary

We shape the geometry of the continental LAB in our model mostly by fitting the intermediate- to long-wavelength Bouguer anomaly, but also by simultaneously maintaining consistency with two independent datasets: The heat flow map of South America of Hamza and Muñoz [1996] and the continental-scale seismic tomography models of Vdovin et al. [1999], van der Lee et al. [2001] and Feng et al. [2004]. To do this, we accept that the LAB beneath the continent is thermally defined as the depth at which the conductive thermal gradient characteristic of the lithosphere intersects an asthenospheric adiabat [e.g. Artemieva and Mooney, 2001] and, therefore, that variations in LAB depth should be positively correlated with the intermediate- to long-wavelength distribution of surface heat flow density *Qs* (see appendix A). In addition and as pointed out by Feng et al. [2004], the sub-crustal seismic velocity structure is primarily sensitive to mantle temperature variations and hence to the LAB depth. During the modelling, we attempted to represent in the final LAB geometry the most robust features suggested by both the regional- to continental-scale variations of *Qs* as reported by Hamza and Muñoz [1996] and the distribution of S-wave velocities below 100 km and Rayleigh surface waves at periods higher than 60 s shown in the maps of Vdovin et al. [1999], van der Lee et al. [2001] and Feng et al. [2004]. The sensitivity analysis presented in section 7 suggests that the average estimated error in the LAB geometry resulting after this modelling is 10 km.

4.5.4. Continental Moho

The depth to the Moho discontinuity, i.e. the crustal thickness of the continental plate, has been fixed in the model based on the results of seismic experiments along some regions of the Andean margin (Fig. 4.4). Most of these data have been produced in the framework of the SFB267 project. Receiver function analysis of locally recorded earthquakes along the Central Andes between 20° and 25°S were published by Yuan et al. [2000, 2002]. Using two different methods, these authors observed a P-to-S seismic wave velocity converter at the base of the continental crust and reported the depth to the continental Moho that has been digitized and included as a constraint in the model. As discussed in the original papers, these estimates are

generally in good agreement with published data obtained from deep seismic refraction profiles [Wigger et al., 1994; Schmitz et al., 1999] and other receiver function studies [e.g. Beck et al., 1996]. However, Yuan et al. [2002] do not discuss the reason why their estimates from a grid-search algorithm are up to 10 km shallower than those reported by Yuan et al. [2000] based on stacking and depth migration of the receiver functions along EW profiles. We used a Moho depth in between these two estimates to represent the Moho geometry along profiles where both results are available.

Yuan et al. [submitted paper] also report a receiver function profile along 39°S, from which we have digitized the Moho depths obtained after correcting the depth-migrated receiver functions by the results of the grid-search method. Two additional unpublished receiver function profiles imaging the continental Moho at 21°S and 25.5°S were provided to us by I. Wölbern (pers. comm.). Fromm et al. [2004] estimated Moho depths from an analysis of apparent Pn wave phase velocities recorded along an EW array of broadband seismic stations around 30°S. These estimates are in good agreement with those published by Regnier et al. [1994] and were also digitized and included into the model.

For unconstrained regions, the Moho was shaped by fitting the intermediate-wavelength Bouguer anomaly along each modelled cross-section, maintaining a smooth transition to seismically constrained regions and following the general trend of surface elevation under the assumption that the orogenic topography is primarily compensated by a crustal root. By doing this, we follow the main conclusions of previous isostatic analyses of the Andes [e.g. Götze et al., 1991 and 1994; Introcaso et al., 1992; Tassara and Yáñez, 2003] and elsewhere [e.g. Lowry et al., 2000; Watts, 2001], but note that we made no attempt to fix the Moho geometry from predictions of either Airy or flexural isostatic compensation models because we want to use this geometry in the future as independent information to quantify the isostatic state.

Based on the previously-mentioned discrepancy between different receiver function methods, the average thickness of converters at the base of the crust along receiver functions profiles, the sensitivity analysis of Fromm et al. [2004] and the results of the sensitivity analysis in section 7, we estimate the average uncertainty in Moho depth to be ±5 km.

4.5.5. Intracrustal density discontinuity

The geometry of the ICD was not constrained by independent information and is simply the result of fitting the observed and calculated Bouguer anomaly at intermediate to short wavelengths. The ICD was conceived as a proxy to map 3D variations in the internal

crustal density structure. However, fixing the geometry of deeper density discontinuities with independent information means that lateral density variations within the mantle that are not represented in the modelled structure should also be incorporated during forward modelling into the geometry of the ICD. However, the results of the sensitivity analysis presented later show that expected lateral variations in mantle density not accounted for in the model have only a minor effect on the ICD geometry compared to the much more important effect produced by crustal density variations.

4.6. Residual Bouguer anomaly and model accuracy

The overall quality and accuracy of the 3D density model resulting from this forward modelling can be quantified by its ability to reproduce the observed gravity field. Fig. 4.5 shows a residual Bouguer anomaly map that was computed after gridding the differences between the observed and calculated Bouguer anomaly for each gravity station contained in the database. Less than 10% of the studied region has residual anomalies with amplitudes higher than the estimated error in the observed Bouguer anomaly (±20 mGal). These anomalies are of very short to short wavelength and they are not systematically distributed in the map. However, some of the extreme misfits, mostly offshore, can be correlated with tectonic features. This correlation demands an explanation and we suggest the following: 1) A concentration of intense positive and negative residual anomalies is evident along the south-western track of the Nazca ridge, as are similar anomalies generally associated with bathymetric highs. The very short wavelength of these features (Fig. 4.1a) means that they are almost impossible to model on cross-sections separated by 1° in latitude; 2) ENE-oriented, long, paired positive-negative anomalies are clearly correlated with modelled cross-sections separating the four southernmost segments of the Nazca plate (Fig. 4.2a). This is due to the fact that the density structure of the mantle lithosphere required to fit the measured Bouguer anomaly near the trench changes abruptly along these cross-sections; 3) Negative residual anomalies can be observed along the trench axis, indicating that material there should have a density considerably lower than the value of 2.7 Mg/m^3 selected for the upper crust.

Despite these short-wavelength residual anomalies, at wavelengths relevant to this work (i.e. greater than some hundred kilometres), the residual anomalies lie well in the range ±20 mGal. The histogram in Fig. 4.5 shows a tight concentration of residual anomaly values around 0 mGal, defining a standard deviation of 15.05 mGal and a correlation factor between measured and calculated anomaly of 1.00.

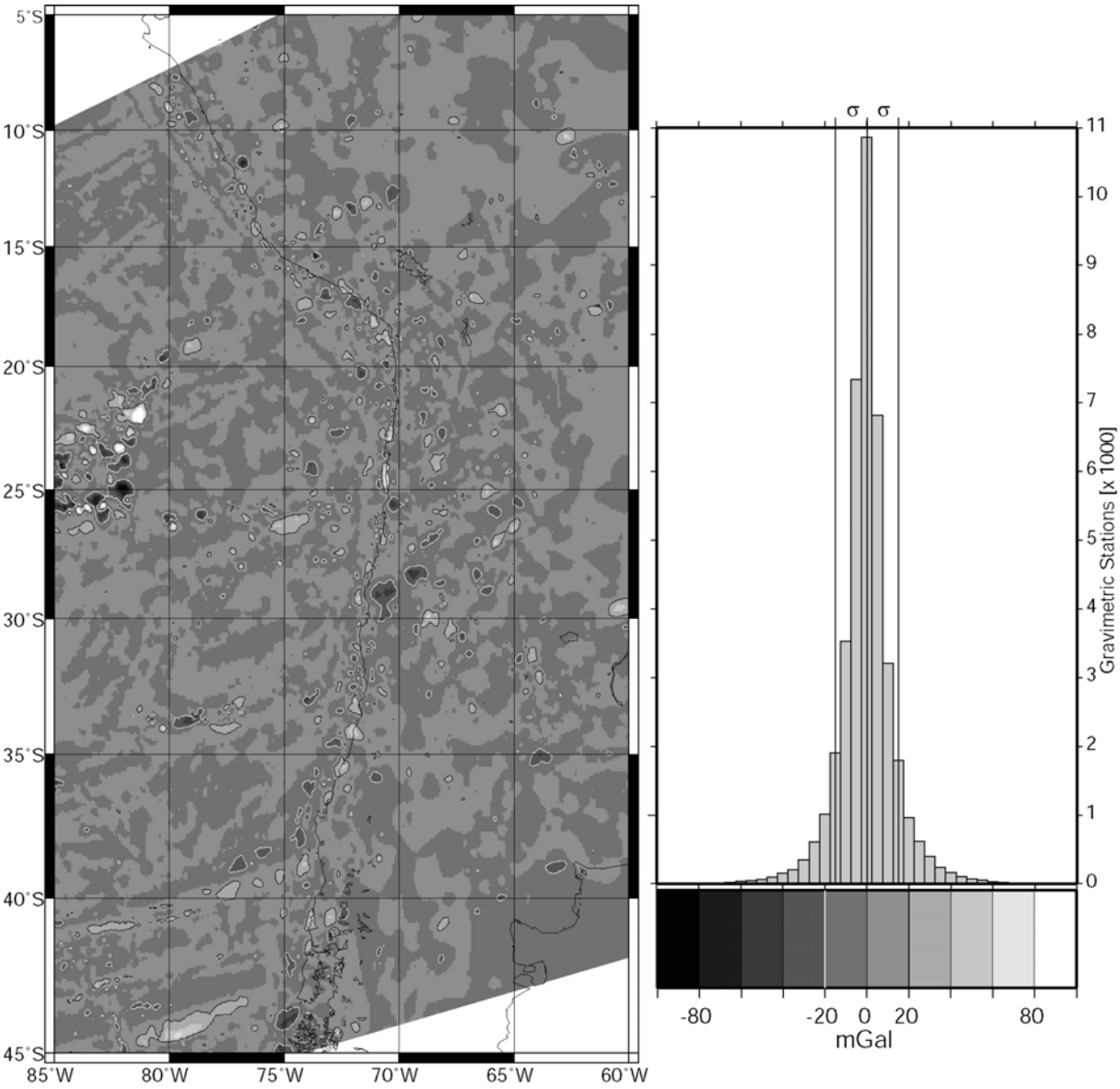

Fig. 4.5. Residual Bouguer anomaly associated to the final model. White contour is for the -20 mGal iso-line and black contour is for the 20 mGal iso-line. The residuals were calculated for each gravimetric station as the difference between observed and modelled Bouguer anomaly. The histogram shows a tight concentration of residuals around zero with a standard deviation σ = 15.05 mGal.

These statistics are good and indicate that the 3D density model satisfactorily reproduces the desired intermediate- to long-wavelength features of the observed Bouguer anomaly with an accuracy better than the error in the measured anomaly: The model is a good representation of the large-scale distribution of mass along the Andean margin.

4.7. Sensitivity analysis as a tool for interpreting the model results

After the final model was produced, we used a facility included in the IGMAS modelling software to test the sensitivity of the model to changes in density and geometry. We estimated the uncertainty in the density selected for each modelled body (Table 1) as the

tolerable percentage variation in this parameter that, *ceteris paribus*, would produce a variation of the calculated Bouguer anomaly equal to the estimated error of the observed anomaly, i.e. ±20 mGal. These uncertainties are presented in the upper panel of Table 2. The average uncertainty in the model resulting from changes in the depth to the main density discontinuities is shown in the lower panel of Table 2. To estimate these uncertainties, for several selected cross-sections of the model we calculate the vertical variation of the vertices defining each discontinuity that produce, *ceteris paribus*, an average change in the calculated Bouguer anomaly equal to the tolerance limit of ±20 mGal. However, the uncertainty associated with each discontinuity should be lower than that of the vertices because the 3D effect on the gravity field produced by vertically moving the whole discontinuity is larger than the effect of moving single vertices. We estimate the expected uncertainty in the depth of each density discontinuity to be 20% of the average uncertainty calculated for single vertices along the selected cross-sections. As a consequence of Newton's law, the uncertainties in density and geometry of the forming bodies increase with depth and decrease as a function of the total mass of the body and the density contrast along each discontinuity.

Table 2: Uncertainties of allocated density values and main geometries resulting from the sensitivity analysis

Densities																			
Segment	Oceanic Plate and Subducted Slab										Continental Plate				Astenosphere			
	m		a		b		c		d									
	OC	OM	OC	OM	OC	OM	OC	OM	OC	OM	UC	LC	WM	EM	OA	LA	WA	EA
I	2.31	0.30	2.95	0.49	5.75	0.96	6.32	0.97	7.07	1.14	0.92	0.32	0.40	0.15	0.06	0.06	0.36	0.23
II	2.00	0.27	3.03	0.42	5.03	0.69	6.39	0.94	8.73	1.25								
III	1.40	0.21	2.78	0.45	3.78	0.50	4.57	0.58	7.63	0.94								
IV	1.37	0.18	3.83	0.51	4.34	0.44	5.48	0.58	7.23	0.77								
V	0.65	0.15	3.60	0.42	4.12	0.41	6.03	0.61	9.85	1.14								
VI	0.85	0.18	1.34	0.42	2.23	0.44	2.42	0.44	7.74	0.80								
VII	2.42	0.21	2.88	0.41	3.59	0.45	3.81	0.47	6.84	7.14								

Geometries					
Oceanic Plate		Slab	Continental Plate		
Moho	LAB	Upper Surface	ICD	Moho	LAB
1.5	8	5	2	5	10

Abbreviations as in Table 1. All values are absolute magnitudes. Uncertainties in density are tolerable percentage change with respect to the density values for the corresponding body in Table 1. Uncertainties in geometries are in km.

The information summarized in Table 2 can be used to analyse the meaning of the final geometry obtained for density discontinuities that are not constrained by independent information. We discuss in the following paragraphs some specific aspects to be taken into account during the description and interpretation of the model.

Densities of the oceanic mantle lithosphere could change by 0.15–0.3% with respect to the selected values (Table 1) without a noticeable change in the modelled Bouguer anomaly. Therefore, the density changes of ~1.5% resulting from compositional variations between the harzburgite and lherzolite used for the calculations in appendix A (Fig. 4A.2a), should be clearly recognized in the model. For a given composition, the model is sensitive to variations in the average density of the lithospheric mantle produced by a change in plate age of ±5 My. Such an age change for the Nazca plate does occur at scales of 500 km and its effect on the gravity field, namely the westward decrease of the Bouguer anomaly caused by decreasing average mantle density, is incorporated into the model by shifting the lithosphere-asthenosphere boundary downward by more than 8 km, i.e. the uncertainty of the depth to this discontinuity (lower panel of Table 2).

For bodies representing the mantle structure underneath the continent, the calculated uncertainties in density between 0.15 and 0.4%, and 10 km in the LAB depth, reflect a tolerable change in the surface heat flow of ±5 mW/m^2 for cold foreland-shield regions and up to ±10 mW/m^2 for hotter orogenic regions (Fig. 4A.2b of appendix A). Along some regions of the Andean margin, the surface heat flow changes at scales smaller than the size of mantle bodies (~200 km) and with amplitudes higher than the estimated tolerance limit (5–10 mW/m^2; Hamza and Muñoz [1996]). These thermal anomalies with respect to the modelled mantle structure could produce a local misfit between observed and modelled Bouguer anomaly that will be compensated during the modelling by shifting unconstrained density discontinuities, i.e. the Moho in regions without seismic constraints and the intracrustal density discontinuity (ICD). The effect on the Moho could be of the order of ±5 km (lower panel of Table 2), which is identical to the uncertainty range in the location of this discontinuity by seismic methods (section 5.4). This indicates that mantle density variations, at least those associated with regional fluctuations in the thermal field, will not cause major additional uncertainties in the Moho geometry. Similarly, such a phenomenon should have a minor effect on the ICD geometry (~2 km, lower panel of Table 2) compared with that caused by lateral density variations within the crust.

The selected density value for the upper continental crust has an uncertainty of 0.92%. Tassara [submitted paper] shows that thermal variations between hot volcanic regions and cold shields at upper-crustal levels (shallower than 20 km depth) could produce up to 0.3% density variation for a given crustal composition. This suggests that our model will not be sensitive to density variations due to changing temperatures within the upper crust. The empirical relationship between density and silica content of crystalline upper crustal rocks

proposed by Tassara [submitted paper] indicates that a 0.92% tolerable change in density is equivalent to a variation of ~5 wt% SiO_2 around the normal content of a granite (73 wt% SiO_2). For regions where the upper crust is mostly formed by crystalline rocks with a composition lying in this range, the geometry of the ICD will be dominated by lateral density variations below the structural base of the upper crust. If the real upper crust is to be locally formed by rocks with density ~1% different to the value of 2.7 Mg/m^3 (sedimentary basins or crystalline rocks with less than 68 wt% SiO_2), then the effect on the Bouguer anomaly will be higher than the tolerance limit of 20 mGal. This effect would be compensated in the model by a vertical shift of the ICD with a magnitude greater than the 2 km estimated as the uncertainty for this discontinuity (Table 2).

A tolerable change of 0.32% for the lower crustal density with respect to the modelled value indicates that the model is sensitive to density variations of up to 2.5% that can be produced by the extreme thermal differences between hot volcanic arcs and cold shields [Tassara, submitted paper]. The huge density uncertainties of ~15% related to the unknown lower crustal composition [Tassara, submitted paper] are even more important. In this context, the geometry of the ICD resulting from the forward gravity modelling reflects the lateral variations in upper and mostly lower crustal composition, temperature within the lower crust and, to a minor extent, local thermal or compositional anomalies in the mantle.

4.8. Description and discussion of results

In this section, we describe the main results obtained from the forward gravity modelling in terms of the final geometry of the density discontinuities that make up the 3D model. Note, however, that geometries partially or completely unconstrained by independent information reflect both the real structure of bodies and also the likely lateral variations in the density of these bodies that is not represented by the initial density structure. During the description of each particular geometry, we emphasize this point when we consider it necessary to guide the reader toward an adequate interpretation of the results. The following description includes a discussion of some significant first-order features evident in the model. This discussion aims to show how the results of this model can be used, within its restrictions, to gain hints on diverse issues related to Andean geodynamic processes. We opt not to extensively interpret these results because we consider this a long-term task to be dealt with in the future in collaboration with other members of the Andean geoscientific community.

4.8.1. Nazca plate

4.8.1.1.Oceanic Moho

The thickness of the oceanic crust obtained from the 3D density model is shown in Fig. 4.6a. This thickness has been calculated by subtracting the resulting oceanic Moho depth from the satellite-derived bathymetry. The Nazca plate seems to have an anomalous crustal thickness with respect to the globally homogeneous value of 7±1 km estimated by White et al. [1992] and Bown and White [1994]. Only ~55% of the area covered by the Nazca plate in Fig. 4.6a has a crustal thickness lying within this tight range. This value reduces to ~45% if the more homogenous region to the north of the Nazca ridge is excluded.

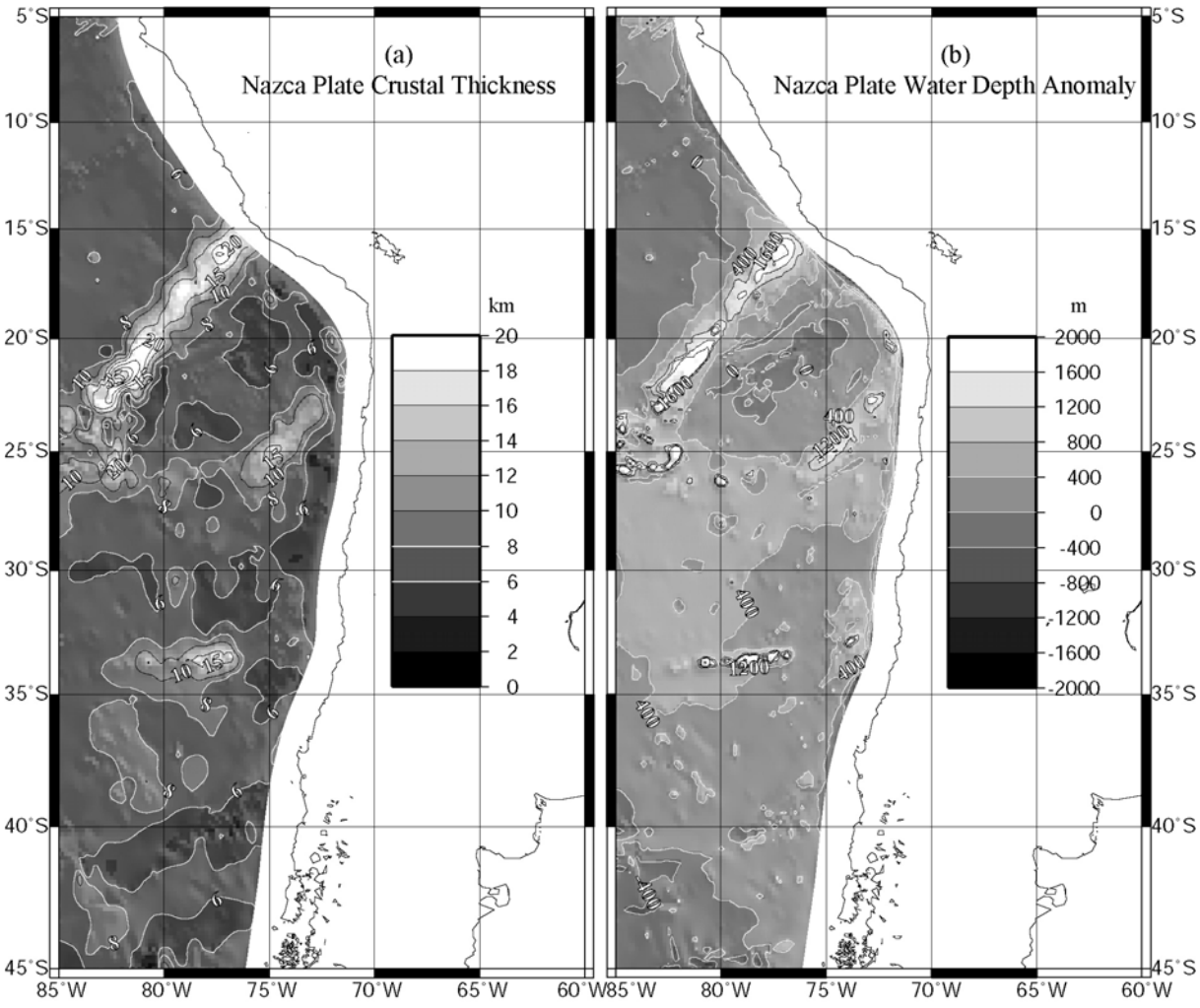

Fig. 4.6. (a) Crustal thickness of the oceanic Nazca plate resulting from the model. Bold white contours are for iso-lines of 6 and 8 km, remarking the worldwide average oceanic crustal thickness of 7±1 km [Bown and White, 1994]. (b) Water depth anomaly of the Nazca plate (see text for definition) for plate ages after Müller et al. [1997].

The anomalous distribution of crustal thickness correlates with the water-depth anomaly (Fig. 4.6b), i.e. the difference between observed bathymetry and water depths

predicted by the plate-cooling model [Turcotte and Schubert, 2002, p. 175] for Nazca ages from Müller et al. [1997]. Regions of the Nazca plate with positive depth anomalies greater than 500 m are generally correlated with estimated crustal thickness greater than 8 km. This correlation suggests that these areas have been both thermally uplifted after interaction with known hotspots (i.e. Easter, San Felix, Juan Fernández) and diffuse thermal anomalies ("Easter hot line" of Bonatti et al. [1977]), and injected with amounts of magma that exceed that generated along the spreading centres. Depth anomalies greater than 1000 m along oceanic ridges are compensated by crustal roots in excess of 10 km thickness. The thickest oceanic crust is observed below the Nazca ridge, which shows a continuous crustal root with maximum crustal thickness of 35 km at the intersection of the ridge with the Nazca FZ. This is more than twice the maximum thickness of the Iquique and Juan Fernández ridges reaching values up to 15 km. The crustal root of this latter feature is discontinuous and has no major thickening toward the trench, in agreement with the gravity-derived crustal thickness observed by Yáñez et al. [2002] and the refraction seismic tomography of Kopp et al. [2004].

Neutral to negative water-depth anomalies are correlated with thin oceanic crust (<6 km) along all fracture zones south of 15°S. Thinner crust along fracture zones is a common observation [e.g. White et al., 1992] reflecting the fact that melting of the mantle at spreading ridges is inhibited by low temperatures [Bown and White, 1994; Henstock and Thompson, 2004]. The thick oceanic crust along the Chile Rise is not likely to be a real structural feature, but more an artefact of the model generated to compensate the presence of light molten material along the active ridge axis whose density should be much lower than the value selected for the crust of segments I and II. This could also be the case for some regions characterized by active intraplate volcanism, like the Juan Fernández archipelago and Sala y Gómez island (26°S, 80°W in Fig. 4.1a), and presumably the south-western track of the Nazca ridge for which the crustal thickness of Fig. 4.6a should be considered an upper bound.

4.8.1.2.Oceanic lithosphere-asthenosphere boundary

The depth to the oceanic LAB obtained from the density model (LAB_M) is shown in Fig. 4.7a. Fig. 4.7b shows the age-predicted LAB depth (LAB_P) calculated from a plate-cooling model. LAB_P decreases and LAB_M increases west of the trench.

As previously commented, the westward deepening of LAB_M was incorporated in the model to reproduce the expected westward-increasing mantle lithosphere mass deficit with respect to the density structure at the trench caused by the decrease in average density related to westward-younging of the Nazca plate.

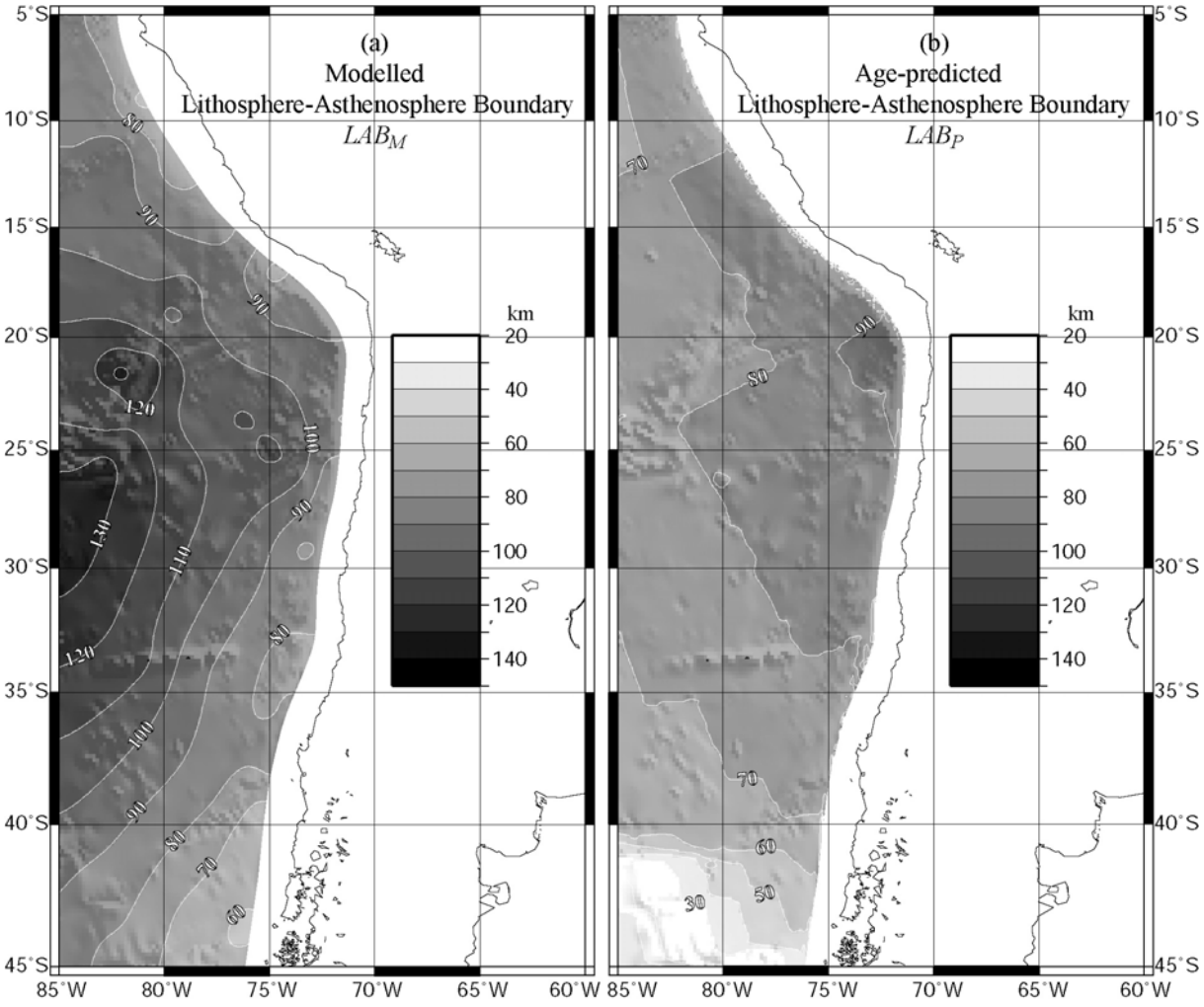

Fig. 4.7. (a) Lithosphere-astenosphere boundary (LAB) of the Nazca plate resulting from the model (LAB_M). (b) LAB depth predicted by an age-dependent plate-cooling model (see text) for Nazca ages after *Müller et al.* [1997].

In this context, the resulting LAB_M map of Fig. 4.7a can be used to predict the oceanic mantle density structure expected under the thermal conditions implied by the plate-cooling model. In appendix B, we explain a method to correct the densities of the oceanic mantle lithosphere considering the values selected for each segment (Table 1) and the maps of Fig. 4.7 for modelled and age-predicted depths to the oceanic LAB. This correction essentially considers that the LAB depth must correspond to the prediction of the plate-cooling model and then the spatial variations of LAB_M are converted to density variations with respect to the selected mantle lithosphere values (Table 1) by means of a simple mass balance (see appendix B). In appendix B we also show that the density structure resulting from this procedure, after being included to the 3D density model, reproduces the observed Bouguer anomaly, demonstrating the validity of such a correction. The corrected densities are shown in panels I

to VII of Fig. 4.8. The spatial variations obtained are now realistic, with a density decrease west of the trench and jumps across the fracture zones separating plate segments. However, unrealistically low density values were calculated for segments younger than 15 My (segment I and western portion of segment II), suggesting that the method described is not valid for extremely thin and hot lithospheres near the melt region of active mantle upwelling along the Chile Rise.

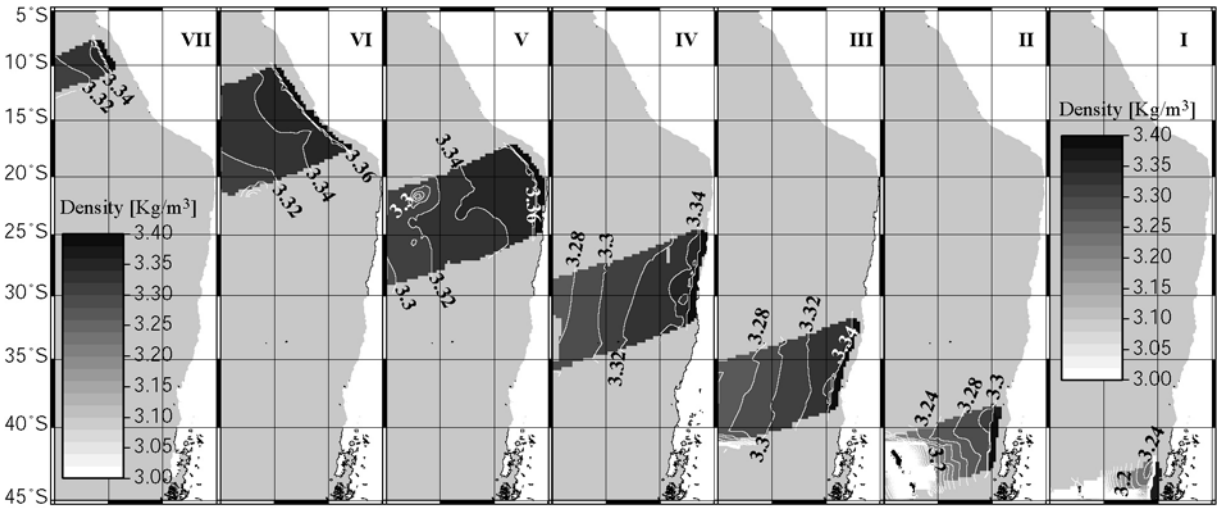

Fig. 4.8. Density structure of the Nazca plate lithospheric mantle. Panels show the results of the procedure discussed in the text and appendix B for each of the seven modelled segments forming the oceanic plate.

At regional scales, reduced densities with respect to the surroundings can be observed along the Nazca ridge, particularly in its south-western part (segment V). This correlates with the thickest oceanic crust estimated from the forward gravity modelling (Fig. 4.6a). Both phenomena are ultimately related to the lowest Bouguer anomaly observed west of the trench region and suggests that, in addition to a thick crustal root, low lithospheric mantle densities also play a role in compensating the load of the Nazca ridge. This in turn could imply a thermally active lithospheric system, at least along the south-western extension of the ridge, that can be associated with the complex and poorly studied interaction of the ridge, the Nazca FZ and some deep thermal anomaly like that proposed by Bonatti et al. [1977]. Small-scale (<100 km diameter) zones of mantle density lower than the surroundings can also be appreciated near the trench to the north of the Juan Fernández ridge (segments IV) and along the subduction region of the Mocha-Valdivia FZ (segment III). The former is in good agreement with both the position and magnitude of reduced mantle seismic velocities observed north of the Juan Fernández ridge by Kopp et al. [2004]. These authors suggest that this is due to the hydration and partial serpentinization of the uppermost mantle that is

enhanced along the bent outer rise region because of the reactivation of an old hotspot-related, pervasive fault pattern. An enhanced mantle serpentinization could also be advocated to explain low densities associated with the subducting Mocha–Valdivia FZ, for which the concentration of strike-slip deformation during its Neogene tectonic history [Tebbens and Cande, 1997] likely left a pervasively faulted uppermost mantle.

4.8.2. Subducted slab

The slab geometry obtained by the method described in section 4.2 is shown in Fig. 4.9a. This is a map with contour lines every 25 km between the trench axis and 410 km depth that, like the other two geometries presented in the same figure, includes shaded digital topography illuminated from the NE to allow a comparison of this geometry with upper plate morphostructure. This figure also shows the location of active volcanoes. Continental-scale features observed in this figure are in good agreement with the slab geometries proposed previously by Cahill and Isacks [1992], Creager et al. [1995] and Gutscher [2002]. In particular, coincidences between these previous models and the geometry resulting from our modelling are observed in the definition of: (1) penetration angle (i.e. between the trench and 50 km depth) with a relatively constant value of ~20° along the region 5° to 36°S, decreasing southward; (2) flat segments between 100 and 150 km depth associated with volcanic gaps in Peru (5°–15°S) and Argentina (27°–32°S); (3) steeply-subducting segments with dip angles of 25–35° between flat-slab regions; (4) a general parallelism between trench axis, coastline, volcanic front and slab depth contour lines along the Arica Bend. However, the slab geometry of Fig. 4.9a contains significant information at regional scales (hundred kilometres) because the database compiled for this model considers more information of better quality compared to previous compilations. The contour lines in Fig. 4.9a were explicitly not smoothed because we wanted to preserve the spatial resolution of 100 km allowed by the spacing between modelled cross-sections.

A quantitative analysis of the slab geometry produced by this model and its correlation with other tectonic features along the continental margin will be presented by Hoffmann-Rothe et al. [submitted paper]. Tassara et al. [2005] advanced an interpretation dealing with the causes of slab flattening in the context of the relationship between the crustal structure of subducting oceanic ridges (Fig. 4.6a), the position and morphology of flat-slab segments and its remarkable correlation with continental plate morphostructure (Fig. 4.9a). These observations suggest that although the southern, shallow part of the Peruvian flat-slab is obviously correlated with the subduction of the huge Nazca ridge, the positive buoyancy of

subducted ridges with respect to the surrounding slab [e.g. *Gutscher et al. 2000; Yáñez et al., 2001] is perhaps a necessary but insufficient condition* for causing slab flattening. In particular, note that the subduction of the Iquique ridge, having a more continuous crustal root than the Juan Fernández ridge in Fig. 4.6a, is associated with a steeply subducting slab underneath the Altiplano region. Two other factors to be considered as controls on the shape of the slab are; 1) the locally enhanced buoyancy of the oceanic plate produced by the hydration of the uppermost mantle to the north of the Juan Fernández ridge, as revealed by seismic velocities [Kopp et al., 2004] and density anomalies (Fig. 4.8, panel IV), and 2) the dynamic control exerted by the absolute westward motion of the South American plate (as pointed out by the thermomechanical models of van Hunen et al. [2004]) coupled with decreasing amounts of convergence absorbed by upper-plate shortening from the Altiplano region toward the Peruvian and Argentinean flat-slab segments [e.g. Kley et al., 1999].

Other interesting aspects revealed by the modelled slab geometry, like its relationship with the internal forearc structure and seismogenic processes, the notably steepening of the slab east of the flat-slab segments, or the decreasing depth to the slab along the Southern Volcanic Zone, are topics to be investigated and discussed in the future.

4.8.3. Continental plate

4.8.3.1.Lithosphere-asthenosphere boundary

The LAB depth below the Andean continental margin resulting from this modelling is shown in Fig. 4.9b. We describe some continental-scale features of the LAB geometry that are robust with respect to the uncertainties derived from the gravity modelling and those related to the heat flow data [Hamza and Muñoz, 1996] and seismic tomography models [Vdovin et al., 1999; van der Lee et al., 2001; Feng et al., 2004] used to constraint it.

Active volcanic zones are underlain by a lithosphere thinner than 80 km. This value reduces to 60 km below the central Puna and along the SVZ south of 36°S, where thinner crust (Fig. 4.9c) allows the existence of shallower asthenosphere. As shown in Plates 2b and 2c, the lithosphere and asthenosphere along volcanic zones are formed by the western bodies of Fig. 4.2b that have a low density with respect to eastern mantle bodies, reflecting their position underneath the hottest and presumably most hydrated regions of the continental margin. The lithosphere below volcanic gaps related to flat-slab segments corresponds to the cold and hence dense eastern body (EM in Fig. 4.2b and Table 1) and is also thicker than 100 km.

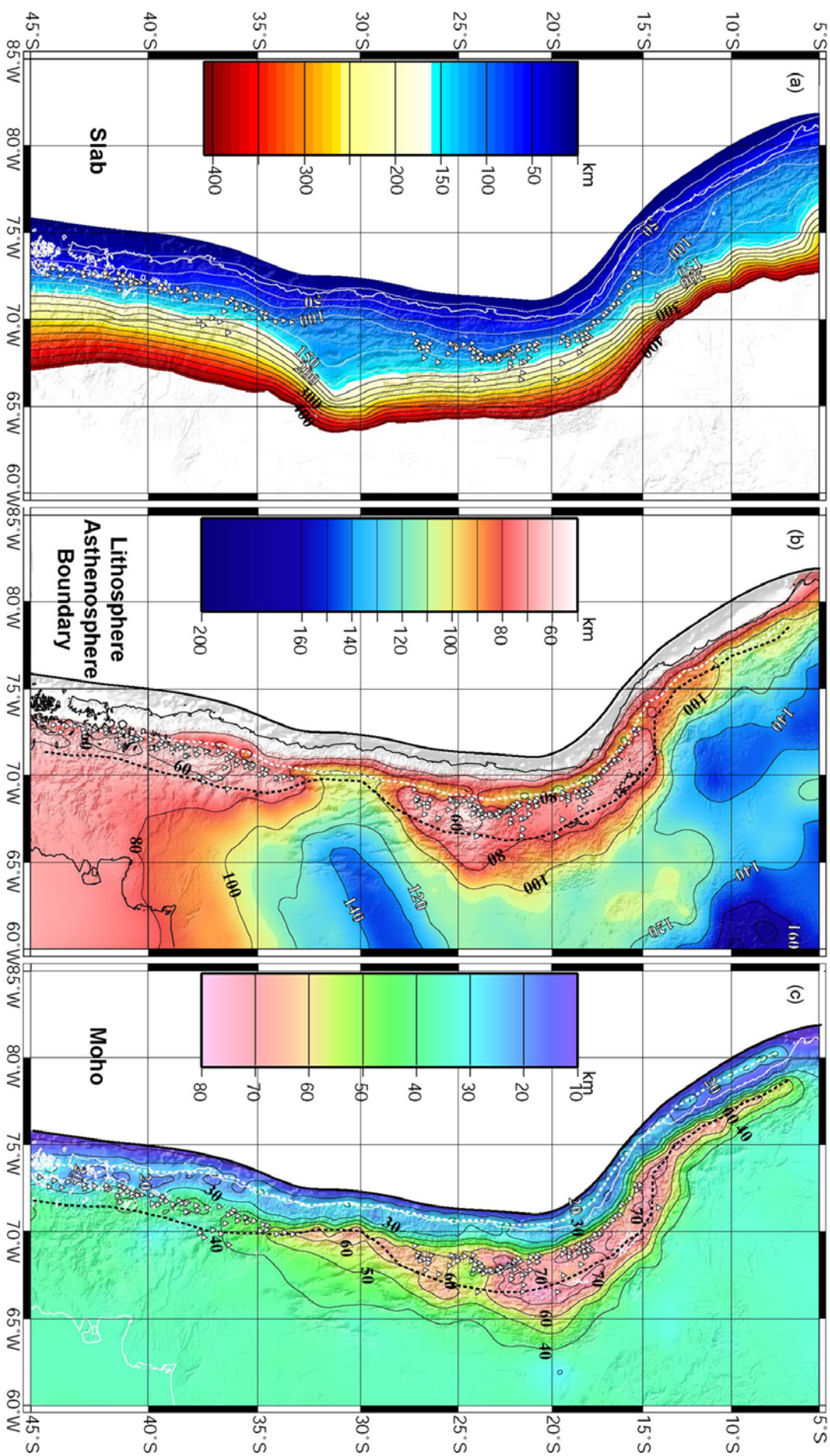
(a)
Slab
km
400
300
200
150
100
50
(b)
Lithosphere
Asthenosphere
Boundary
km
200
160
140
120
100
80
60
(c)
Moho
km
80
70
60
50
40
30
20
10
5°S
10°S
15°S
20°S
25°S
30°S
35°S
40°S
45°S
85°W
80°W
75°W
70°W
65°W
60°W

Fig. 4.9. (Previous page) Geometry of density discontinuities underneath the continental margin that were constrained with independent data. Triangles are active volcanoes and the shading corresponds to topography-bathymetry. (a) Subducted slab contoured every 25 km. (b) Lithosphere-astenosphere boundary (LAB) contoured every 20 km. (c) Moho every 10 km. In (b) and (c), dotted lines depict the intersection of the corresponding discontinuity with the subducted slab (white line) and the plane separating western and eastern mantle bodies (black line) (see also Fig. 4.2b).

East of the main cordilleras, the LAB reaches depths greater than 120 km north of 12°S and along an ENE-oriented region underneath the eastern Sierras Pampeanas. The northwestern limit of the latter lithospheric domain roughly correlates with the presumed suture between the Rio de la Plata Craton and the Pampean suspect terrain, and between the latter and the Cuyania terrain [e.g. Ramos, 1988; Chernicoff and Zappettini, 2003]. This suggests a first-order distinction between these lithospheric blocks. The thickest lithosphere within the study region (>160 km thick) underlies the eastern exposed sector of the Brazilian shield. This region is separated from the thick lithosphere underneath the Peruvian foreland (>140 km thick) by a NW-oriented and relatively thin lithospheric corridor that is well-defined both by low seismic velocities [van der Lee et al., 2001; Feng et al., 2004] and high heat flow values [Hamza and Muñoz, 1996]. This region connects with a wide zone of lithosphere thinner than 120 km underlying the western Brazilian shield and the foreland behind the Altiplano-Puna plateau.

For regions not affected by arc volcanism, the thinnest lithosphere can be recognized east of the Southern Andean cordilleras underneath the North Patagonian Massif, where LAB depths are less than 80 km. This region shows a gradual transition to the thick Pampean lithosphere to the north resembling NW-oriented structures that can be recognized in the topography of the western Sierras Pampeanas and underlying the Neuquén System and San Rafael Block (see Fig. 4.1a). This could also suggest that the proposed Patagonian plate [e.g. von Gosen, 2003] is different to the continental blocks to the north. The region of shallow LAB in Patagonia east of the Neuquén System and along the northern part of the North Patagonian Massif has been subjected to intense Cenozoic volcanic activity of presumed asthenospheric origin [e.g. de Ignacio et al., 2001; Kay et al., 2004]. This could be related to a persistent thermal anomaly that characterizes the Patagonian lithosphere.

4.8.3.2.Moho

The depth to the continental Moho is shown in Fig. 4.9c. In the following, we comment on some continental-scale characteristics of this geometry that, within the

uncertainties previously discussed, can be considered first-order features of Andean crustal thickness.

The modelled intersection of the continental Moho with the subducted slab along the Central Andean forearc (white dashed line in Fig. 4.9c) roughly coincides with the coastline, the 0 mGal contour line (Fig. 4.1b), the 30–50 km depth range of the subducted slab (Fig. 4.9a) and the downdip limit of the seismogenic zone (DSZ) as defined by Tichelaar and Ruff [1991] and Khazaradze and Klotz [2003]. Thus, the model suggests a strong causative relationship between these observables and also supports the main conclusion of Oleskevich et al. [1999] that the DSZ corresponds to the intersection of the subduction thrust fault with serpentinized, non-seismogenic forearc mantle. Along the Southern Andean forearc (mostly south of 38°S), the modelled Moho-slab intersection is shifted westward with respect to the DSZ location of Khazaradze and Klotz [2003]. This could indicate a seismogenic forearc mantle in this region similar to that proposed for other subduction zones [e.g. Simoes et al., 2004]. However, this cannot be considered a robust interpretation implied by the forward gravity modelling because other forearc configurations are also possible, but in this case they must be compensated by changes in either the density or the geometry of bodies forming the forearc region. Given the importance of having the best possible knowledge of the structure of the seismogenic zone for assessment of the seismic and tsunami hazard along this highly-populated forearc, we believe that a systematic test of different slab-forearc configurations incorporating independent information into our model should be carried out in the future.

East of the Moho-slab intersection, the crust is commonly thinner than 30 km and the Moho is upwardly convex. The forearc mantle is generally shallower than 20 km, particularly underneath the Peruvian coastline and the Central Valley south of 38°S. This latter feature is consistent with seismic tomography results that image a mantle upwelling below the Southern Andean forearc [Bohm, 2003] and with Meso-Cenozoic extension of the forearc region [e.g. Mpodozis and Ramos, 1989; Vietor and Echtler, submitted paper].

The high topography of the Central Andean orogen is compensated by thick crust that reaches more than 60 km thickness. This crustal root seems to be very narrow (<100 km) north of 13°S, widening southward as the Altiplano also widens. This part of the plateau is locally underlain by crust thicker than 70 km. The maximum crustal thickness of ~75 km constrained by receiver function analyses (Fig. 4.4) has been identified beneath the western limit of the Eastern Cordillera. As observed by other authors [e.g. Wigger et al., 1994], the Atacama Basin (Fig. 4.1a) is underlain by an abnormally thick crust for its comparatively low elevation with respect to the surrounding plateau [Yuan et al., 2002]. In contrast to the thick

Altiplano, the Puna shows a thin crustal root up to 55 km thick. Considering that the elevation here is almost 1000 m higher than in the Altiplano, Yuan et al. [2002] proposed that the Puna is partially compensated by a thermal root related with the shallow mantle asthenosphere that we also observe in the resulting LAB map (Fig. 4.9b). These features are consistent with the Late Neogene delamination event suggested by some authors [e.g. Kay and Kay, 1993; Allmendinger et al., 1997] and restricts the occurrence of significant lower crustal removal to a region located in the central part of the Puna.

South of 26°S the high cordilleras are again underlain by a Moho deeper than 60 km. The morphology of the crustal root along the southern Central Andes seems to be affected by the complex structural interaction between the Frontal Cordillera, the Argentinean Precordillera and western Sierras Pampeanas (Fig. 4.1a), further suggesting the presence of lithospheric-scale discontinuities between different continental terrains. Fromm et al. [2004] pointed out that the crust below the two latter morphostructures is considerably thicker (45–55 km) than what can be expected for their relatively low and discontinuous elevation, suggesting significantly high densities either for the lower crust or the underlying mantle. The resulting ICD geometry presented in the next section favours the former interpretation. Along the Principal Cordillera, the crustal thickness gradually decreases from 60 to 40 km. The region underlain by crust thicker than 40 km is bordered by the eastern boundary of the San Rafael Block. Around 36°S, we observe a local minimum of the crustal thickness that can be connected with a NW-oriented region of thin crust (<35 km) to the east. This region was constrained by receiver function results at 39°S (see Fig. 4.4) and is correlated with upper crustal structures recognisable in topography and associated with active back-arc volcanism [e.g. *Folguera et al.*, 2002; *Kay et al.*, 2004]. The central segment of the SVZ (37°–40°S) overlies crust ~40 km thick, but this value seems to decrease to less than 30 km along the southern-most SVZ. In this southern-most region there are no seismic constraints and the shallow Moho could be indicating the presence of dense mantle and/or crustal material.

The regional-scale variations in crustal thickness suggest that, although the main compensation mechanism supporting the variations in elevation seems to be related with thick and buoyant crustal roots [e.g. Götze et al., 1991; Introcaso et al., 1992; Tassara and Yáñez, 2003], other mechanisms (mantle thermal roots, elastic flexure, lateral density variations, dynamic support) could be acting to partially compensate the mountain chain. Crustal thickness is the primary signal of large-scale deformation processes occurring at the continental margin [e.g. Isacks, 1988; Hindle et al., 2005] and in this context, our model offers for the first time an integrated view of variations in deformation processes along the

entire Central and Southern Andean segments. However, understanding deformation processes at this continental-scale should consider the internal crustal structure that can be inferred from the intracrustal discontinuity contained in our model.

4.8.3.3.Intracrustal discontinuity

The depth to the ICD obtained from this forward gravity modelling is shown in Fig. 4.10a. This is an unconstrained density discontinuity that was shaped by fitting the intermediate- to short-wavelengths of the Bouguer anomaly not accounted for by subcrustal structure. The geometry of the ICD is a result of our model that is completely independent of other geoscientific information and can, therefore, be used to gain interesting and new insights into the three-dimensional mass distribution within the Andean continental crust. The sensitivity analysis discussed previously indicates that the ICD geometry primarily represents lateral density variations produced by the changing composition both of the upper and lower crust and by temperature variations at lower crustal depths, with a minor effect induced by compositional and thermal mantle anomalies with respect to the modelled structure. Thus, the interpretation of ICD geometry is a complex task that should be undertaken with the assistance of independent information that allows a qualitative, or hopefully quantitative, separation of these phenomena.

In an attempt to evaluate the effect of upper crustal density variations due to the surface geology, we produced a map showing the percentage difference of surface density with respect to the value of 2.7 Mg/m^3 selected for the modelled upper crust. This map was generated using the digital geological map of South America at 1:5.000.000 scale [Schobbenhaus and Bellizzia, 2001], which describes the lithology of geological units with relatively little detail. For instance, the database differentiates between volcanic and plutonic rocks with acid-intermediate and basic-intermediate compositions, the grade of metamorphic rocks and age of sedimentary sequences. Applying standard density values for the described lithologies [e.g. Carmichael, 1989; Tassara, submitted paper] and then calculating for each geological unit the percentage difference with respect to 2.7 Mg/m^3, we ended up with the map shown in Fig. 4.10b. Due to the way in which this map was constructed, it should be used with caution and mostly to analyse continental-scale features contained in the ICD geometry.

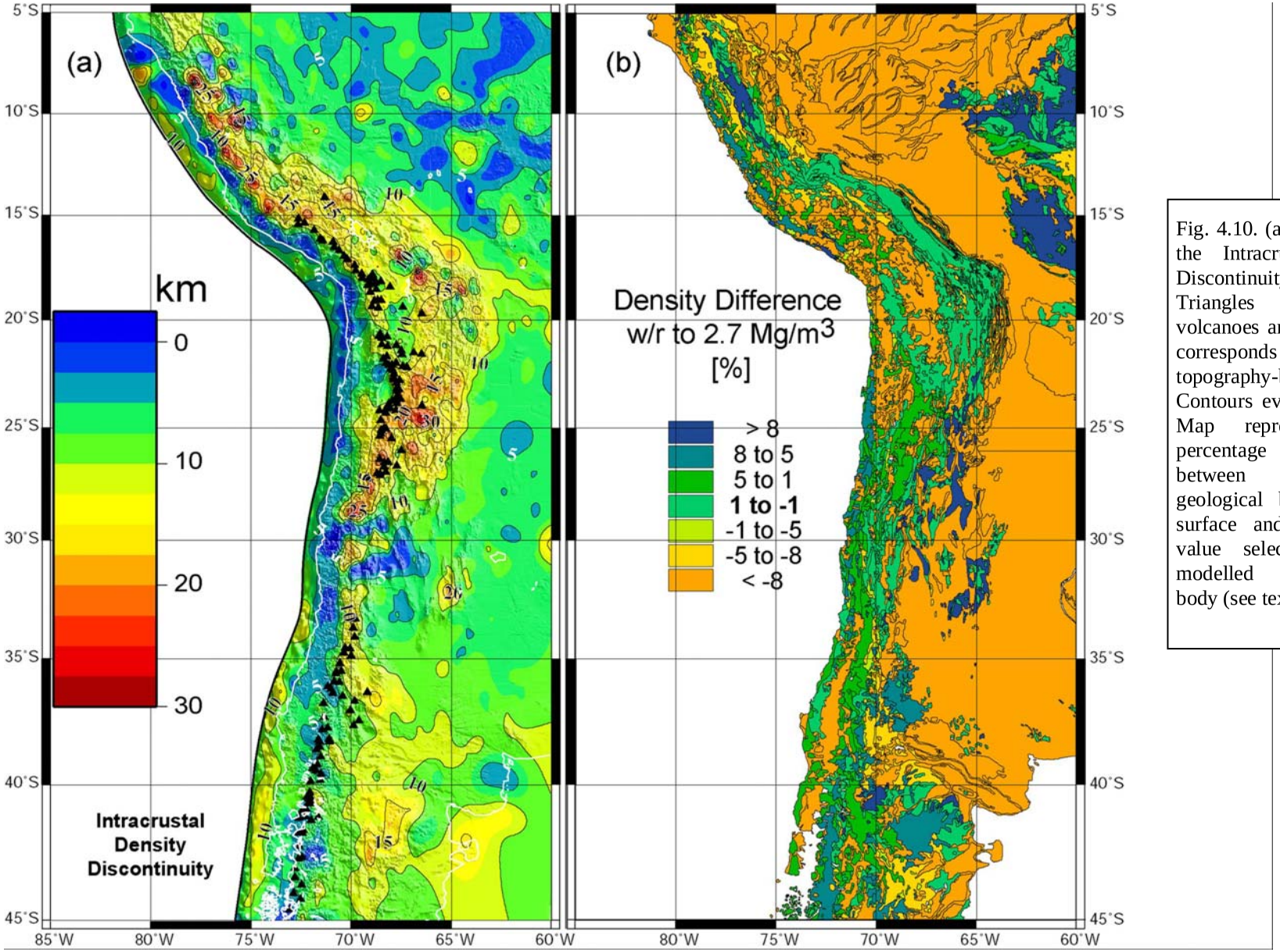

Fig. 4.10. (a) Geometry of the Intracrustal Density Discontinuity (ICD). Triangles are active volcanoes and the shading corresponds to topography-bathymetry. Contours every 5 km. (b) Map representing the percentage difference between density of geological bodies at the surface and the density value selected for the modelled upper-crustal body (see text).

With consideration of the restrictions associated with the procedure used to obtain the geometry of the ICD and those related with the construction of the surface density map, we advance a general interpretation of some interesting features evident in Fig. 4.10. As is suspected, we note a general anti-correlation between the depth to the ICD and surface density. For instance, in regions where high-density rocks are exposed at the surface, the resulting geometry of the ICD is shifted upward by an amount that should depend on the volume of these units. Cenozoic basaltic lavas covering the eastern Neuquén System and North Patagonian Massif, which have a high density at the surface (5-8% higher than 2.7 Mg/m^3 in Fig. 4.10b), coincide with regions where the ICD is deeper than 10 km. This suggests that they are relatively thin sheets overlying a basement likely dominated by the Late Palaeozoic rocks associated with the Choiyoi felsic province [e.g. Mpodozis and Ramos, 1989]. Meso-Cenozoic, intermediate to basic igneous rocks outcropping along the Central Andean Coastal Cordillera and the Patagonian Cordillera are characterized in Fig. 4.10b by densities higher than the value of 2.7 Mg/m^3 selected for the upper crustal body. These rocks are consistently associated with an ICD depth shallower than 5 km (Fig. 4.10a). The spatial continuity of this shallow-ICD zone indicates that such high density rocks likely form the entire crust along the Central Andean forearc (including its offshore region) and that they could be connected with the Patagonian Batholith below the Cenozoic cover of the northern-most Southern Andes. Similarly, the Early Palaeozoic, high-density, mafic to ultramafic rocks outcropping along some of the western Sierras Pampeanas (Valle Fértil and Pie de Palo) seem to be the surface expression of a large terrain characterized by ICD depths shallower than 7.5 km and hence presumably by high crustal densities underneath the Bermejo and Mendoza basins, the Precordillera and parts of the Frontal Cordillera. The extent of this region in Fig. 4.10a coincides with the presumed location of the suspected Cuyania terrain [Ramos, 1988; Chernicoff and Zappettini, 2003], supporting its characterization as a mafic-dominated block probably allocthonous with respect to the dominantly felsic Andean basement [e.g. Lucassen et al., 2004]. However, the ENE-oriented nature of regions where the ICD is shallower than 5 km and their correlation with seismic velocity anomalies at mantle depths, as imaged by Wagner et al. [2005], suggest that this ICD feature could be partially associated with strong lateral density variations along the upper mantle likely produced by the subduction of the Juan Fernández ridge.

For a robust interpretation of these examples, the likely effect of low temperatures in increasing the density of crustal rocks along the forearc and the Argentinean flat-slab should be also considered. In the latter case, temperatures as low as 500°C at ~60 km depth [e.g.

Gutscher, 2002] could favour the eclogitization of lower crustal rocks and their subsequent densification with respect to deep warmer regions near active volcanic arcs. The analysis of Tassara [submitted paper] indicates that even in this case, the lower crustal composition must be more mafic than an andesite because felsic compositions are not able to generate high density eclogites at lower crustal depths that can produce the shallow ICD characterizing this region. In this scenario, a shallow ICD above the Argentinean flat-slab should be considered as the result of both mafic material forming the crust and low temperatures at lower crustal levels.

Fig. 4.10b also shows that most of the rocks outcropping along the Central Andean orogen have a density differing from the modelled upper crustal value by a magnitude similar to the tolerable uncertainty of this body, i.e. ±1% (Table 2). For this region, the ICD geometry should reflect the structural discontinuity between upper and lower crust and the variations of the lower crustal density with respect to the value selected for the model. In this context, one of the strongest features observed in Fig. 4.10a is an ICD generally deeper than 15 km between 7° and 29°S underneath the axis of the Central Andean orogen, reaching values higher than 25 km to the north and south of the Altiplano. This deep ICD suggests a large felsic component in the orogenic crust, at least larger than beneath the cordilleras south of 36°S, where an ICD shallower than 10 km points toward a mafic-dominated crust. Note that heat flow data [Hamza and Muñoz, 1996] and the geometry of the lithosphere-asthenosphere boundary in Fig. 4.9b suggest a thermal state that along the Central Andean plateau and the Principal and Patagonian Cordilleras is likely characterized by high temperatures at lower crustal depths. This precludes a possible thermal effect in generating the observed difference in the ICD geometry for these regions and supports a compositional cause. Interpretation of elastic thickness (Te) estimates [Tassara and Yáñez, 2003; Tassara, 2005a] predicted that, in addition to along-strike variations in crustal thickness and in the thermomechanical regime, such a contrast in the crustal composition is necessary to explain Te values lower than 10 km along the Central Andes and higher than 30 km south of 38°S. Something similar has been suggested by Sobolev and Babeyko [2005] based on a thermomechanical modelling of the Andean orogeny. The resulting ICD geometry seems to confirm this general predictions and allows the suggestion that the contrasting crustal structure between the Central and Southern Andes is a primary factor in controlling the strength of the continental margin and therefore its capability to deform in response to tectonic forces. The rigid mechanical behaviour induced by a bulk mafic crust for the Southern Andes could be responsible for the particular tectonic evolution of this segment where little crustal shortening is recorded [e.g. Kley et al.,

1999; Vietor and Echtler, submitted paper]. A relatively weak, felsic-dominated crust in the Central Andes likely promotes the concentration of compressive deformation that leads to the construction of this huge mountain belt. The geological structure associated with this crustal compositional pattern (Fig. 4.10b) provides evidence for a long-term control on Andean segmentation by old continental features.

Variations in ICD geometry along the Central Andean plateau correlates with changing foreland deformation mechanisms. A shallower ICD along the central Altiplano (10–15 km) coincides with the flat detachment of the thin-skinned Sierras Subandinas, whereas toward the boundaries of the plateau, a deeper ICD (>15 km) correlates with thick-skinned deformation [Isacks, 1988; Allmendinger and Gubbels, 1996; Kley et al., 1999]. This particular geometry, combined with an uncorrelated pattern of crustal thickness (Fig. 4.9c), could indicate an upper–lower crustal decoupling and lower crustal flow of likely molten material along the axis of the plateau as envisaged by Yang et al. [2003], Husson and Sempere [2003], Hindle et al. [2005] and Gerbault et al. [2005]. An ICD no deeper than 25–30 km along the Altiplano-Puna plateau suggests that the bulk crustal composition is not felsic, as suggested by some authors interpreting low P-wave velocities (Vp ~6 km/s) at middle-lower crustal depths [e.g. Beck and Zandt, 2002; Yuan et al., 2002]. As proposed by Schmitz et al. [1997], the combination of low Vp and high density at lower crustal depths underneath the plateau could be interpreted in terms of substantial degrees of partial melting of a mafic protolith. This is because partial melting strongly reduces the seismic velocities of rocks while having only a minor effect on their density. The coincidence of high seismic attenuation (Qp = 100) and an extremely high electrical conductivity (1 S/m) down to 20 km depth below the Altiplano [e.g. Haberland et al., 2003 and references therein] has been interpreted as a distinctive signal of high degrees of partial melting in the middle and lower crust. This partially molten lower crust could also explain the low rigidity underneath the Altiplano [Tassara and Yáñez, 2003; Tassara, 2005a] and is consistent with the low bulk viscosity of the lithosphere (10^{19}–10^{22} Pa s) required to produce the crustal flow thought to be partially responsible for the deformation path along the plateau [Lamb, 2001; Yang et al., 2003; Husson and Sempere, 2003; Hindle et al., 2005; Gerbault et al., 2005]. We believe that the three-dimensional results of our model could be combined in the future with available seismic velocity models in order to estimate the amount and distribution of partial melting present in the Altiplano and Puna crust.

4.9. Summary and Conclusions

We have presented a 3D density model covering the Nazca plate (85°W) and the Andean continental margin (60°W) between Northern Peru (5°S) and Patagonia (45°S) that incorporates a simplified, but useful, representation of density structure to 410 km depth. This 3D structure is the result of forward modelling of the Bouguer anomaly that was constrained by an compilation of independent (mostly seismic) data. This database helps to fix the geometry of the subducted Nazca slab, locally the Moho of the oceanic and continental crusts, and indirectly the lithosphere-asthenosphere boundary underneath the continental plate. The allocation of density values for the bodies forming the model was supported by a quantitative analysis that considers density to be a function of the chemical and mineralogical composition of rocks and the pressure-temperature conditions appropriate for the Andean geodynamic setting. A sensitivity analysis of the model allows a quantification of the uncertainties associated with the modelling and gives a tool to interpret the meaning of unconstrained density discontinuities.

At continental to regional scales, the Bouguer anomaly generated by the final 3D density model reproduces the observed Bouguer anomaly with great accuracy. The average misfit between observed and modelled Bouguer anomalies has a standard deviation of ±15.05 mGal around zero, which lies within the error of the measured Bouguer anomaly (±20 mGal). A discussion of the geometry of the major density discontinuities within the model leads to the following main conclusions:

Nazca Plate

1) The oceanic crustal thickness shows a heterogeneous spatial distribution, with less than 55% of the study area lying in the tight range of 7±1 km identified by White et al. [1992] as the worldwide average. The Nazca ridge has an extremely thick crustal root (>25 km) compared with the thin (<15 km) and discontinuous Iquique and Juan Fernández ridges.
2) Oceanic crustal thickness variations seem to be correlated with significant water-depth anomalies with respect to the plate-cooling model, and can be further related with thermal and/or compositional anomalies in the mantle lithosphere.
3) A density structure for the mantle lithosphere was obtained by a mass balance between the modelled lithospheric thickness and that predicted by a plate-cooling model. The results suggest that anomalously light lithospheric mantle is associated with some

portions of oceanic ridges and exists near the trench axis north of the Juan Fernández ridge and the Mocha–Valdivia fracture zone.

Subducted Slab

1) A preliminary analysis of flat-slab morphology and its correlation with upper plate morphostructure and the crustal structure of subducted ridges suggests that, although the southern Peruvian flat-slab is clearly associated with the subducted Nazca ridge, the subduction of the Juan Fernández ridge perhaps is an insufficient condition for the formation of the huge Argentinean flat-slab. This is because the similarly sized Iquique ridge doesn't correlate with any flat-slab segment. Other factors to be considered are enhanced hydration of crust and uppermost mantle and dynamic coupling with a westward advancing and structurally heterogeneous continental plate that absorbs part of the convergence by decreasing amounts of shortening away from the Altiplano region.
2) The Nazca slab geometry, along with the other geometries resulting from this contribution (in particular for the Moho and the intracrustal density discontinuity along the forearc), could be used in the future, for example, to perform a detailed analysis of the seismogenic zone structure that is important for assessing the seismic and tsunami hazard along the highly populated Andean forearc.

Continental Margin

1) The depth to the lithosphere-asthenosphere boundary (LAB) obtained from the model is shallower than 80 km along active volcanic zones and deeper than 100 km along volcanic gaps associated with flat-slab subduction. The thickest lithosphere (>160 km) is observed underneath the eastern Brazilian shield.
2) An ENE-oriented zone of deep LAB (>120 km) in western Argentina seems to be correlated with the limit between the Rio de la Plata craton and the suspected Pampia terrain. Similarly, a gradual decrease of the lithospheric thickness from the Pampean region toward the North Patagonian Massif supports a difference in the nature of the Patagonian terrain (or plate after von Gosen [2003]) with respect to the continental blocks to the north. The extremely thin lithosphere observed in this region (<80 km) could be associated with the thermal anomaly that produced the Cenozoic alkaline volcanism characteristic of Patagonia.

3) The Central Andean orogen is primary compensated by a crustal thickness greater than 60 km. The Moho depth reaches maximum values of ~75 km along the eastern-central part of the Altiplano plateau. A region of crustal thickness less than 55 km underneath the Puna can be correlated with a proposed recent lower crustal delamination [e.g. Kay and Kay, 1993].

4) Variations in the morphology and thickness of crustal roots underneath the high Andean cordilleras and their relation with topography and amounts of crustal shortening suggest large- and small-scale variations in the isostatic mechanisms that compensate the mountain chain. These variations should be quantified in the future in order to gain knowledge of the processes that construct and support the Andean orogen.

5) The geometry of the intracrustal density discontinuity (ICD) separating felsic upper crust from intermediate to mafic lower crust in the model is perhaps the most interesting result of this contribution. This is because it is a representation of the three-dimensional mass distribution within the continental crust that results exclusively from the forward gravity modelling (no independent constraints were used). The interpretation of the ICD geometry requires the use of independent information to allow the separation of effects produced by changing upper-crustal geology from compositional and thermal variations in the lower crust. A surface density map obtained from a digital geology database helps to isolate the effect of near surface density variations.

6) The ICD geometry indicates that dense Meso-Cenozoic magmatic rocks exposed at the surface along the Central Andean forearc are also likely to form the offshore forearc and could be connected below the Central Valley to similar rocks that form the axis of the Patagonian Cordillera south of 38°S.

7) A zone of shallow ICD correlates with the location of the suspected Cuyania terrain [Ramos, 1988], supporting an allocthonous origin for this terrain with respect to the more felsic autochthonous Andean basement. However, high crustal densities implied by the ICD geometry could at least partially be the expression of low temperatures produced by the flat subduction.

8) The Central Andean Plateau is dominated by an ICD significantly deeper (> 15 km) than along the Southern Andean Cordilleras (< 10 km). Under similar thermal conditions, this observation suggests a first-order difference in the crustal composition associated with the old geological structure of the continent. This pre-existing

difference likely controls differences in the integrated strength of the margin that in turn can help to explain the long-term Andean segmentation.

9) The deepening of the ICD observed toward the north and south of the Altiplano can be associated with the changing deformation mechanisms observed at the surface and the likely lower crustal flow that acts to help build this mountain belt. The presence of high density material at middle-lower crustal depths can be reconciled with low seismic velocities if the crust is formed by mafic rocks retaining substantial amounts of melt. Partial melting is consistent with interpretations of other geophysical images and helps to explain the low rigidity and viscosity associated with the Central Andean Plateau.

We believe that the 3D density model we presented here is a useful contribution to the Andean geoscientific community. The 3D structure is the final result of the modelling effort we carried out, but we consider the model to be a basis for moving toward an integrated understanding of Andean geodynamic processes.

4.10. Acknowledgements

This project has been possible thanks to many colleges from South America (Diana Comte, Mario Pardo, Jaime Campos, Arturo Belmonte, Denizar Blizkow), Europe (Sergio Barrientos, Tony Monfret, Antonio Villaseñor, Uwe Meyer, Ingo Wölbern) and USA (Robert Fromm), who provide us with original, mostly unpublished data. Daniel Melnick is specially thanked for his assistance with the GIS-based analysis of continental morphostructure. We benefited from fruitful discussions with Rick Allmendinger, Marcelo Farías, Suzanne M. Kay, Stephen Kirby, Constantino Mpodozis, Onno Oncken, Victor Ramos, Stephan Sobolev and Manfred Strecker. This work was supported by the German Collaborative Research Center SFB267 “Deformation Processes in the Andes” funded by the Deutsche Forschungsgemeinschaft. AT’s Ph. D. project at the Freie Universität Berlin is supported by a scholarship from the German Academic Exchange Service (DAAD).

Appendix A: Mantle density structure

To examine the density structure of the mantle, we use the Excel Macro released by Hacker and Abers [2004]. This tool implements the work of Hacker et al. [2003a] to calculate several physical properties (including density) of a predefined mineral assemblage at a given pressure-temperature (PT) condition. This tool was modified to read physical conditions from an one-dimensional PT gradient in order to calculate density profiles downward the lithosphere. Pressures are defined by a lithostatic gradient:

$$P(z) = \rho g z \qquad \text{(A1)},$$

where z is depth, ρ = 3 Mg/m^3 is an average density and g = 9.8 m/s^2 is acceleration of gravity. Lithospheric temperatures are calculated along conductive geotherms. For the oceanic plate the geotherm follows a plate-cooling model [Turcotte and Schubert, 2002, p.161]:

$$T_{OC}(z) = \Delta T\left[\frac{z}{z_{L0}} + \frac{2}{\pi}\exp\left(-\frac{\kappa\tau\pi^2}{z_{L0}^{\ 2}}\right)\sin\left(\frac{z\pi}{z_{L0}}\right)\right] \qquad \text{(A2)},$$

where ΔT = 1300°C is the temperature difference between top and bottom of the oceanic lithosphere, $z_{L0} = 2.32(\kappa\tau)^{0.5}$ is the thermal thickness of the plate, κ = 1 mm^2/s is the thermal diffusivity and τ is the age of the oceanic plate. The continental thermal structure is defined by a conductive geotherm with crustal heat production decaying exponentially with depth [Turcotte and Schubert, 2002, p.147]:

$$T_{CT}(z) = Ts + \frac{Qs - \rho Hl}{k}z + \frac{\rho Hl^2}{k}(1 - e^{-z/l}) \quad \text{(A3)}$$

Ts = 25°C is the surface temperature, H = 1 μW/m^3 is the crustal heat productivity, l = 10 km is the length scale for the decrease of H with depth, k = 2.5 W/m°C is the thermal conductivity and Qs is surface heat flow density. This parameterisation defines the one-dimensional thermal structure of the oceanic lithosphere $T_{OC}(z)$ by the age of the oceanic plate τ, and that of the continental lithosphere $T_{CT}(z)$ by the surface heat flow density Qs. Examples of these geotherms are shown in Fig. 4A.1 for an oceanic plate age of 30 My and a continental

heat flow of 50 mW/m^2. As discussed in the main text, these are the thermal conditions representing the reference model into the forward gravity modelling.

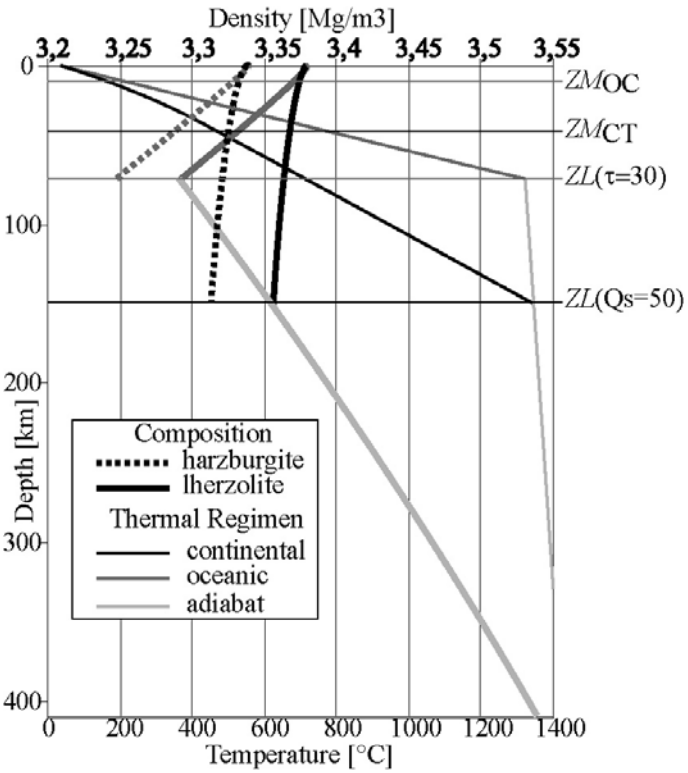

Fig. 4A.1. Density profiles (thick lines) calculated as explained in the text for harzburgite (dotted line) and lherzolite (bold line), and temperature gradients (thin lines) for three thermal regimes: continental (black), oceanic (grey) and adiabatic (light grey). This colour code also holds for the density profiles. ZM is depth to the Moho (OC=oceanic; CT=continental) and ZL depth to the lithosphere-astenosphere boundary ("τ=30" means oceanic plate age of 30 My; "Qs=50" means continental surface heat flow of 50 mW/m^2).

The asthenospheric thermal regimen is defined by an adiabat described by:

$$T_A(z) = T_0 + Gz \qquad \text{(A4)},$$

where T_0 = 1300°C is the potential temperature reached at the Earth surface and G = 0.3°C/km is the adiabatic gradient.

Fig. 4A.1 also shows density profiles calculated by coupling equations (A1) to (A4) with the macro of Hacker and Abers [2004] for two mineral assemblages; a spinel harzburgite ("hzG" in Hacker and Abers [2004]) and a garnet lherzolite ("pyrolite" in Hacker and Abers [2004]). These rocks represent mantle peridotites characterizing respectively depleted continental lithosphere and fertile asthenosphere. The oceanic lithosphere, which is the residue left after much less amounts of basalt extraction than that producing the continental lithosphere [e.g. Lee et al., 2005], would have an intermediate mineralogical composition between these end-members. From these density profiles we calculate an average lithospheric mantle density:

$$\overline{\rho} = \frac{1}{ZL - ZM}\int_{ZL}^{ZM} \rho(z)dz \qquad \text{(A5)}$$

with $\rho(z)$ being the variation of density with depth resulting from the computations and *ZM* and *ZL* the depth to the Moho and to the lithosphere-astenosphere boundary (LAB), respectively. The latter is defined as the intersection of the conductive lithosphere gradient with the asthenospheric adiabat. Applying this procedure for oceanic plate ages between 5 and 50 Myr, continental surface heat fluxes between 45 and 85 mW/m^2 and *ZM*=10 km for the ocean and *ZM*=40 km for the continent, we compute variations of the average lithospheric density $\overline{\rho}$ for both selected peridotites as a function of τ and *Qs*. This is presented in Fig. 4A.2 that also shows the variations of *ZL* and the average densities of a pyrolite along the adiabat representing the asthenosphere. The latter was calculated with an expression similar to (A5), but integrating between *ZL*=75 km (= LAB depth for a 30 Myr old oceanic lithosphere) and *ZL*(τ) in Fig. 4A.2a, and between *ZL*=150 km (= LAB depth beneath a continent conducting a surface heat flow of 50 mW/m^2) and *ZL(Qs)* in Fig 4A.2b.

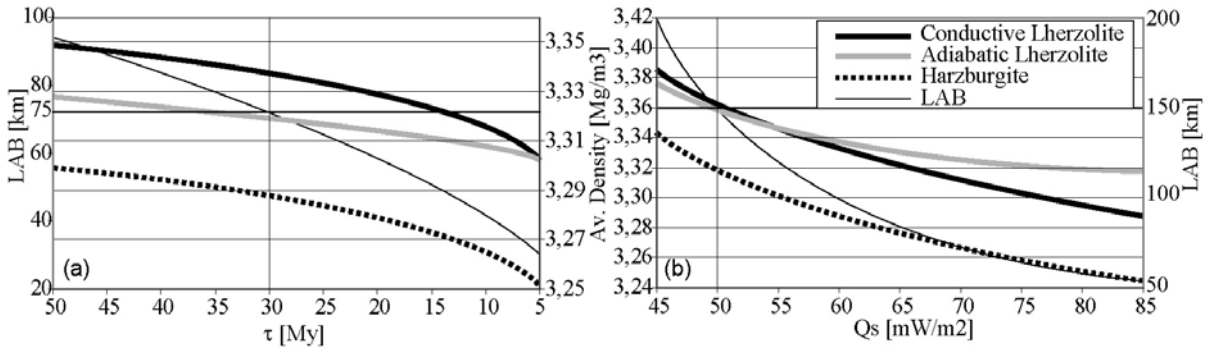

Fig. 4A.2. Average density (thick lines) of the mantle and depth to the lithosphere-astenosphere boundary (thin line) calculated as explained in the text for two mantle peridotites as a function of (a) oceanic plate age and (b) continental surface heat flow.

Information in Fig. 4A.2 was used to design the reference model and to select density values for the bodies forming the 3D density model, as discussed in the main text.

Appendix B: Correcting the density structure of oceanic mantle lithosphere

Fig. 4B.1 represents, schematically and in a 2D section, the relationship between the constant density of the oceanic mantle lithosphere selected for the forward gravity modelling ρ_M, the asthenospheric density ρ_A, the depth to the lithosphere-astenosphere boundary (LAB) resulting from the forward modelling LAB_M (Fig. 4.7a), the LAB depth predicted by a plate-cooling model LAB_P (Fig. 4.7b; see appendix A for computation of LAB from the plate-cooling model) and the corrected density for the oceanic mantle lithosphere $\rho_P(x)$ that we want to calculate from the other parameters. The three latter magnitudes depend on the distance x from the trench axis.

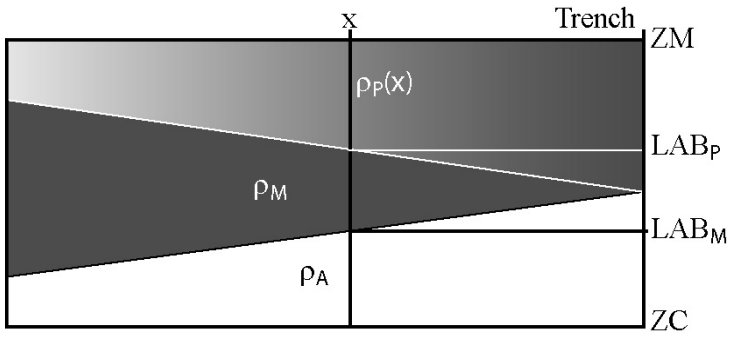

Fig. 4B.1. Schematic representation of the relationship between the lithospheric mantle structure of modelled oceanic plate and that expected for the plate-cooling model. x = distance from the trench axis, ρM = density of the modelled lithospheric mantle body, ρA = density of the modelled asthenospheric mantle body, ZM = depth to the oceanic Moho, LAB_P = depth to the lithosphere-astenosphere boundary predicted by the plate-cooling model, LAB_M = depth to the lithosphere-astenosphere boundary from the model, ZC = an arbitrary compensation depth, ρp(x) = predicted density of the lithospheric mantle as a function of x. This parameters are used to compute a mass balance expressed by equations B1 and B2.

By construction of the 3D density model, at x=0 we have that $LAB_M = LAB_P$ and $\rho_M = \rho_P(x)$. For $x \neq 0$, a balance of the total mass contained in vertical columns of the modelled density structure and that expected for an age-dependent plate-cooling model of the oceanic plate allows the following expression to be written:

$$\rho_M\left[LAB_M - ZM\right] + \rho_A\left[ZC - LAB_M\right] = \rho_P(x)\left[LAB_P - ZM\right] + \rho_A\left[ZC - LAB_P\right] \qquad \text{(B1)},$$

where ZM is the depth to the oceanic Moho resulting from the gravity modelling (Fig. 4.6a) and ZC is a compensation depth. Arranging this expression and considering the three-dimensional nature of the problem, we get:

$$\rho_P(x,y) = \frac{\rho_M\left[LAB_M(x,y) - ZM(x,y)\right] + \rho_A\left[LAB_P(x,y) - LAB_M(x,y)\right]}{LAB_P(x,y) - ZM(x,y)} \quad \text{(B2)},$$

where (x,y) denote the geographic coordinates of the evaluating point in a map. $LAB_P(x,y)$ (Fig. 4.7b) was computed by the procedure discussed in appendix A and considering the oceanic plate ages for the Nazca plate extracted from the grid of Müller et al. [1997]. This information was used together with the results of the 3D density model for the depth to oceanic Moho ZM(x,y) (Fig. 4.6a) and $LAB_M(x,y)$ (Fig. 4.7a) and density values summarized in Table 1 for the lithospheric and sub-lithospheric oceanic mantle, to compute the corrected density values $\rho_P(x,y)$ from (B2) for each of the seven segments of the Nazca plate considered in this study (Fig. 4.2a). The results of these calculations are shown in Fig. 4.8.

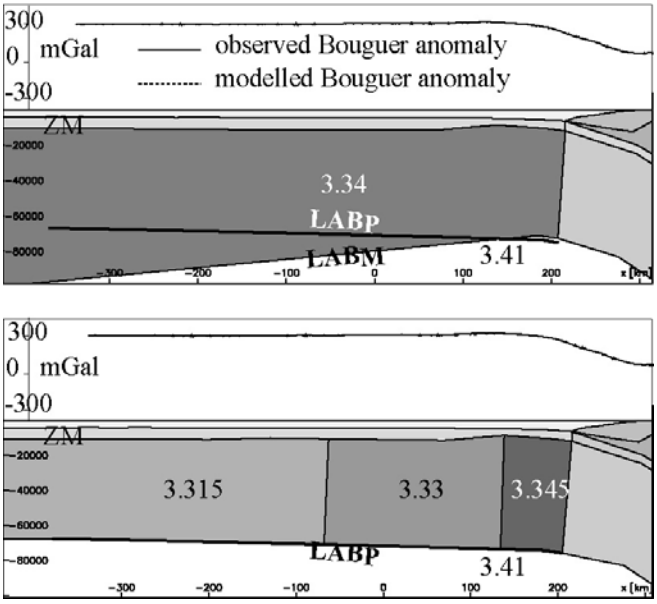

Fig. 4B.2. Upper panel: part of a vertical cross-section from the 3D density model along segment VII of the Nazca plate. Note the good fit between observed and modelled Bouguer anomaly and the geometries and values of parameters defined in Fig. B1. Lower panel: the same cross-section but with a lithospheric mantle structure corrected after applying the procedure of eq. B2. Note that the fit to the gravity field is as good as in the upper panel.

In order to test the validity of such a procedure, we modified the density structure of the 3D model for the segment VII of the Nazca plate to coincide with that predicted by (B2). The upper panel of Fig. 4B.2 shows a detail for one of the cross-sections forming the segment VII in the original 3D density model. Note the good fit between observed and modelled Bouguer anomaly and the similarity with the situation schematised in Fig. 4B.1, in particular that the mantle lithosphere is formed by one body of constant density, and that LAB_M and LAB_P diverge westward the trench axis. The lower panel of this figure shows the same cross-section but now the mantle lithosphere has been divided in three different bodies according to the density values and distribution resulting for the proposed procedure and presented in Fig. 4.8, panel I. Using this corrected structure for the lithosphere, fixing the LAB depth to that

predicted by the plate-cooling model (LAB_P) and maintaining the rest of the density structure as defined initially by the 3D density model, it can be observed that the fit between observed and modelled Bouguer anomaly remains as good as for the original situation in the upper panel. This demonstrates that the procedure we use to compute corrected densities for the oceanic mantle lithosphere is valid and generates a density structure that reproduces the gravity field.